ACADEMIC PRESS

Available online at www.sciencedirect.com

SCIENCE DIRECT®

Journal of Computational Physics 186 (2003) 317–355

JOURNAL OF COMPUTATIONAL PHYSICS

www.elsevier.com/locate/jcp

Near-wall LES closure based on one-dimensional turbulence modeling

Rodney C. Schmidt [a,*], Alan R. Kerstein [b], Scott Wunsch [b], Vebjorn Nilsen [c]

[a] *Computational Sciences Department, Sandia National Laboratories, Albuquerque, NM 87185, USA*
[b] *Combustion Research Facility, Sandia National Laboratories, Livermore, CA 94550, USA*
[c] *Lawrence Livermore National Laboratory L-039, Livermore, CA 94550, USA*

Received 5 September 2001; received in revised form 29 July 2002; accepted 9 October 2002

Abstract

A novel near-wall LES closure model is developed based on a revised form of the one-dimensional turbulence (ODT) model of Kerstein and is tested by performing LES calculations of turbulent channel flow at Reynolds numbers based on friction velocity ranging from 395 to 10,000. In contrast to previous models, which invoke Reynolds averaging, near-wall velocity fluctuations and turbulent transport are simulated down to the smallest scales, and can be compared directly to DNS data. Thus, the approach provides more than just a boundary condition. Rather, it is itself a complete (although simplified) model for the wall-normal profiles of velocity within the near-wall region. LES/ODT coupling is bi-directional and occurs both through the direct calculation of the subgrid turbulent stress by temporally and spatially filtering the ODT-resolved momentum fluxes (up-scale coupling), and through the LES-resolved pressure and velocities impacting the ODT behavior (down-scale coupling). The formulation involves finely resolved ODT lines that are embedded within each wall-adjacent LES cell – denoted the inner region. LES cells that are within approximately one LES filter width of the inner region belong to an overlap region where both ODT and LES modeling is active. All other cells are treated using a standard LES approach. Although more expensive than simpler models, the cost of the model relative to the LES portion of the simulation scales favorably with problem size, leading to computationally affordable simulations even at relatively high Reynolds numbers.

Keywords: Turbulence; LES; ODT; Near-wall closure; Channel flow

1. Introduction

The large eddy simulation (LES) approach to computing turbulent flows has seen a veritable renaissance in recent years due to the availability of faster computers, new modeling approaches, and a continued desire for higher fidelity predictive capabilities [22,41]. In contrast to Reynolds-averaged Navier–Stokes (RANS)

* Corresponding author.
E-mail address: rcschmi@sandia.gov (R.C. Schmidt).

0021-9991/03/$ - see front matter © 2003 Published by Elsevier Science B.V.
doi:10.1016/S0021-9991(03)00071-8

methods, whose basic equations are derived by ensemble or time averaging, the LES equations are obtained by applying the idea of spatial filtering. Thus the equations are time dependent and allow for the large-scale three-dimensional unsteadiness that is a vital feature of many engineering and environmental flows. However, the relative computational cost of LES reflects this difference, and LES is in general significantly more expensive than RANS simulations.

To close the LES equations, a subgrid model is required in order to capture the effects of unresolved turbulent motions on the resolved flow scales. The fidelity required of a subgrid model to achieve acceptable overall predictions depends upon several factors, including the fineness of the resolved mesh, the type of problem being solved, and what aspects of the particular flow are important.

For turbulent flows with solid (i.e., no-slip) walls, the subgrid closure problem in the near-wall region is a difficult problem for several reasons. First, uniform filtering becomes ill defined in the near-wall region if the filter width at a given point extends beyond the wall boundary. This introduces mathematical ambiguities that are difficult to reconcile. Second, the dynamics of the flow near the wall are strongly anisotropic, and turbulence production in this region is associated with an up-scale energy cascade that is largely dominant over the commonly assumed down-scale energy cascade that is present elsewhere. Finally, the dominant flow scale at a given distance from the wall is of the order of that distance. Thus, the 'large eddies' that must be captured on the mesh to perform an accurate LES shrink in size as one approaches the wall, leading to excessive computational costs. Several authors have estimated how this resolution requirement scales with Reynolds number, including Chapman [10] (who looked primarily at aerodynamic boundary layers), and Baggett et al. [3] (who focus on turbulent channel flow). These analyses show that the number of grid points required for proper LES resolution of the near-wall region scales approximately as the square of the Reynolds number – a constraint that makes near-wall resolved LES at moderate to high Reynolds numbers unfeasible using present computational resources. To some extent the computational expense can be mitigated by resolving only the near-wall region with a fine mesh. This requires non-uniform meshing techniques coupled with accurate numerics and LES models designed for non-uniform meshes. Although recent work has demonstrated some success in this area (see [29,39]), the computational expense is still quite large, especially for higher Reynolds number flows.

The objective of wall modeling is to provide an approach that in some simplified manner adequately approximates the near-wall effects while avoiding the overwhelming computational expense of resolving the near-wall flow structures. Various models have been proposed and tested, and the recent literature contains several summaries and reviews that provide greater detail than can be presented here (see, for example [6,9,11,37,41]). The first LES wall model was proposed by Deardorff [13] who considered a coarse LES of plane channel flow at infinite Reynolds number. This model imposed conditions on the second derivative of the velocity at the first near-wall grid point such that the plane-averaged velocity profile at this same location satisfied a log law in the mean. Results did not compare particularly well with data, but as has been pointed out [37], this was probably due as much to the poor mesh resolution as to defects in the model.

In 1975 Schumann [42] introduced the first member of a family of approaches, called wall-stress models by Cabot and Moin [9], that share several key characteristics and that are commonly used today. As with Deardorff's model, the near-wall region is not resolved by the mesh. However, instead of imposing conditions on the velocity, a wall-stress boundary condition is imposed at the wall. In Schumann's original model, the mean wall shear stress $\langle \tau_w \rangle$ was assumed known (from the driving pressure gradient), and the instantaneous shear seen by the LES at any point in time is computed as

$$\tau_{12}(x,z) = \frac{\langle \tau_w \rangle}{\langle \bar{u}(x, Y_m, z) \rangle} \bar{u}(x, Y_m, z), \tag{1}$$

$$\tau_{23}(x,z) = \nu \frac{\bar{w}(x, Y_m, z)}{Y_m}, \tag{2}$$

where Y_m denotes the distance between the wall and the first near-wall node, ν is the kinematic viscosity, u and w denote the streamwise and spanwise velocities respectively, an overbar denotes an LES-resolved quantity, and $\langle\cdot\rangle$ denotes a time average.

Schumann's original model is constrained by having to know the mean shear stress a priori, and thus has limited use. Extensions that overcome this have been developed by proposing different simplified models for the flow within the inner region (i.e., the domain between the wall and the first near-wall node), and different couplings with the outer flow conditions. This was first done by Grotzbach [19] who assumed that the mean velocity between the wall and the first LES grid point satisfied a logarithmic law of the wall, such that

$$\langle \bar{u}(x, Y_m, z) \rangle = u_\tau \left[\frac{1}{\kappa} \ln(Y_m u_\tau / \nu) + B \right], \tag{3}$$

where u_τ is the friction velocity ($= \sqrt{\tau_w}$), κ is the Von Karman constant, B is the value of the log law intercept, and in this context $\langle\cdot\rangle$ denotes an average over a plane parallel to the wall. Solving for u_τ (typically an iterative process) allows one to compute the shear stress at the wall. Eq. (1) can then be applied to complete the model. Subsequent variations and refinements of this approach have been suggested by Mason and Callen [31], Piomelli et al. [38], and Hoffman and Benocci [21].

An alternative, more sophisticated wall-stress model was suggested by Balaras et al. [4,5] and also studied by Cabot [6,7]. Called a two-layer model by its authors, the idea is to replace Eq. (3) with a transient form of the thin boundary-layer equations, which are assumed valid in the inner region. Following Cabot and Moin [9], the model equations for the two horizontal velocities can be written as

$$\frac{\partial \tilde{u}_i}{\partial t} + \frac{\partial}{\partial x_j}(\tilde{u}_i \tilde{u}_j) + \frac{\partial \bar{P}_m}{\partial x_i} = \frac{\partial}{\partial y}\left[(\nu + \nu_t) \left(\frac{\partial \tilde{u}_i}{\partial y} \right) \right], \quad i = 1, 3, \tag{4}$$

where continuity is used to find the wall-normal velocity

$$\tilde{u}_2 = -\int_0^y \left(\frac{\partial \tilde{u}_1}{\partial x_1} + \frac{\partial \tilde{u}_3}{\partial x_3} \right) \mathrm{d}y \tag{5}$$

and the tilde is used here to denote the velocities computed using the boundary-layer equations. $\bar{P}_m$ is the near-wall pressure computed from the LES equations (assumed to be independent of y in the inner region), and boundary conditions are imposed at the wall ($\tilde{u}_i(0) = 0$) and at the nearest LES grid point ($\tilde{u}_i(Y_m) = \bar{u}_i(Y_m)$). The eddy viscosity ν_t is computed using algebraic damping functions based on mixing-length theory, with different authors preferring different models [5,6].

On application, a refined one-dimensional mesh that extends from the wall to the first LES grid point is embedded within the LES mesh. Eq. (4) is numerically solved at each LES time step, the shear stress at the wall explicitly calculated and its value specified as a boundary condition for the LES equations.

A more recent modeling approach that differs significantly from the wall-stress models is based on the idea of merging LES with RANS to model the near-wall region [2,35]. Called the detached eddy simulation (DES) approach, this can be viewed as an extension of an idea suggested by Schumann [42]. However, instead of using a simple mixing-length based eddy viscosity, these models use more sophisticated procedures to compute the near-wall eddy viscosity. In the near-wall region the equations reduce to transient RANS equations and turbulent transport is accounted for primarily through an enhanced diffusion mechanism. Away from the wall the equations take on the form of a traditional LES with a gradient-diffusion subgrid closure model. This approach has similarities to the two-layer wall-stress model of Balaras

et al. [5] in that the very near wall region in both approaches is modeled with a set of transient-RANS type equations. (In [37] they are both called zonal models.) In the DES approach, the transition from the near-wall RANS domain to the outer-flow LES domain is continuous, while in the wall-stress model there is a discrete jump between regions.

Figs. 1(a) and (b) illustrate the conceptual regions defined in the wall-normal direction by wall-stress models and by the DES model.

In summarizing the current state-ot-the-art of wall modeling, Piomelli and Balaras [37] point out that although significant progress has been made, the need for continued work in this area remains. For simple flows in which the near-wall behavior is known to follow a prescribed form, algebraic wall-stress models are attractive because they are relatively easy to implement, are computationally inexpensive, and produce reasonable results. However, for more general and complex configurations, the simple models are neither well suited nor well tested. Zonal models (i.e., the two-layer model and the DES approach) have shown improved results in cases where equilibrium laws fail but where the flow is driven by the outer-layer dynamics. In general they suggest that current wall models tend to be accurate only when the inner/outer-layer interaction is one-way, with the outer-layer dynamics providing the dominant forcing.

This limitation is understandable in light of the fact that all current LES wall models, either explicitly or implicitly, consider the inner layer in a Reynolds-averaged sense. Thus, near-wall turbulent velocity fluctuations are suppressed, and the proper dynamic coupling between the wall and the bulk flow is difficult to achieve. In addition, we note that near-wall flows of interest may also be subject to multiphysics processes (thermally induced property variations, gravitational and other body forces, multiphase couplings, etc.) whose dynamic interactions with the bulk flow also can not be captured by currently available wall treatments.

The new approach developed here is significantly different from previous models. It is based on coupling the outer flow LES equations to a revised form of the one-dimensional turbulence (ODT) model of Kerstein [25]. A key attribute of the ODT based approach is that near-wall velocity fluctuations are not suppressed, but are in fact a fundamental aspect of the model itself. In addition, the approach provides more than just a boundary condition. Rather, it is itself a complete (although simplified) model for the velocity (and in principle all associated scalars) within the near-wall region. Finally, the near-wall model dynamics are intimately coupled with the dynamics of the outer-flow LES, allowing for two-way interactions.

Fig. 1(c) illustrates how the near-wall region is conceptualized in the LES/ODT approach in comparison with wall-stress (1a) and DES (1b) approaches. In the near-wall region, an ODT mesh that is finely resolved in the wall-normal direction is embedded within a coarse LES mesh. The ODT evolution equations (described later) capture fine-scale temporal and spatial variations (in one direction) of the three-component

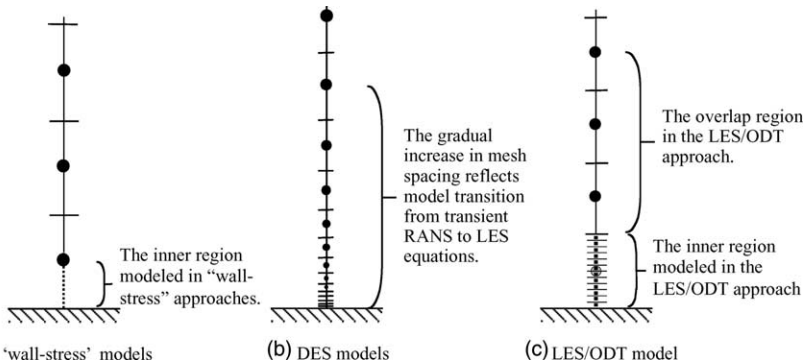

Fig. 1. Conceptual regions and illustrative wall-normal discretization for different LES near-wall models.

velocity field. From a geometric standpoint, one can see that the current model has strong similarities to the two-layer wall-stress model – which also applies an embedded mesh in an inner region (that, in this case, extends only to the first LES mesh point). However, the equations governing the LES/ODT inner region are fundamentally different. For example, the present model does not apply gradient-diffusion-based ideas (e.g., an eddy-viscosity model) for the turbulent transport in this region. In ODT, turbulent transport is simulated through a sequence of fluid-element rearrangements (called eddy events) that occur at multiple length scales and frequencies. In addition, the LES/ODT coupling is strongly bi-directional, and occurs not only at a specific distance from the wall (i.e, as a boundary condition), but throughout an overlap region that extends upwards from the wall through several LES control-volume widths.

The remainder of the paper is organized into five parts. Sections 2 and 3 provide brief descriptions of both the conceptual framework and governing equations of the ODT and LES modeling approaches, respectively. Section 4 describes a coupled LES/ODT model for use in the near-wall region of an LES. Section 5 presents the results of applying the coupled LES/ODT model to fully developed turbulent channel flow at Reynolds numbers based on friction velocity ranging from 395 to 10,000. Section 6 is a concluding discussion of various points relevant to the the new modeling approach and the direction future development is expected to take.

2. Overview of ODT

ODT is a method for simulating, with full spatial and temporal resolution, the turbulent transport and dynamic fluctuations in velocity and fluid properties that one might measure along a one-dimensional (1D) line of sight through an actual 3D turbulent flow. In the 1D dynamical system defined by the ODT model, the effects of turbulent 3D eddies associated with real fluid flow are captured by 1D fluid-element rearrangement events (called eddy events) that occur over a range of length scales with frequencies that depend on event length scales and instantaneous flow states. ODT is an outgrowth of the linear-eddy model [24], in which fluid motions are prescribed without explicit introduction of a velocity field or dependence on the instantaneous flow states. The first ODT formulation [25] involved simulation of a single velocity component evolving on a line. A more recent formulation [27] introduced the evolution of the three-component velocity vector on the 1D domain. Generalization to treat variable-density effects dynamically has been demonstrated [1]. For the work presented in this paper, the formulation described in [27] is adopted as a starting point. Only an abbreviated description of the model is included here, with constant density assumed for simplicity, and the emphasis is on those aspects most relevant to the LES subgrid model described later. In addition, the numerical implementation of ODT for stand-alone calculations (i.e., no multidimensional grid, a single ODT line spanning the channel) of turbulent channel flow is briefly described, together with representative results. This is done in order to demonstrate how the model constants are determined and to give context to its more restricted use as a subgrid model.

2.1. Modeling approach

The version of ODT utilized here describes the evolution of a three-component vector velocity field $v_i(y,t)$ defined on a one-dimensional domain (parameterized by the spatial coordinate y, corresponding to the direction $i = 2$). Additional scalar fields $\theta(y,t)$ may also be defined in the model, but are not implemented here.

The fields defined on the 1D domain evolve by two mechanisms: (1) molecular diffusion, and (2) a sequence of instantaneous transformations, denoted 'eddy events,' which represent turbulent stirring. Each eddy event may be interpreted as the model analog of an individual turbulent eddy. The location, length scale, and frequency of eddy events are determined by a non-linear probabilistic model explained in

Section 2.2. Of note here is that each event is characterized by three properties, a length scale, a time scale, and a measure of kinetic energy, and that a key physical input to the model is a postulated relationship among these quantities that is analogous to the usual dimensional relationship applied to individual turbulent eddies.

During the time interval between each eddy event and its successor, molecular diffusion occurs, governed by the equations

$$\left(\partial_t - \nu\partial_y^2\right) v_i(y,t) = 0, \tag{6}$$

$$\left(\partial_t - \kappa\partial_y^2\right) \theta(y,t) = 0, \tag{7}$$

where ν is the kinematic viscosity and κ is the scalar diffusivity.

In the current formulation, each eddy event consists of two mathematical operations. One is a measure-preserving map representing the stirring motions associated with a notional turbulent eddy. The other is a modification of the velocity profiles in order to implement energy transfers among velocity components. These operations are represented symbolically as

$$\begin{aligned} &v_i(y) \to v_i(f(y)) + c_i K(y), \\ &\theta(y) \to \theta(f(y)). \end{aligned} \tag{8}$$

According to this prescription, fluid at location $f(y)$ is moved to location y by the mapping operation, thus defining the map in terms of its inverse $f(y)$. This mapping is applied to all fluid properties. The additive term $c_i K(y)$ affects only the velocity components, and is used to capture pressure-induced energy redistribution among velocity components.

The functional form chosen for $f(y)$, called the 'triplet map', is the simplest of a class of mappings that satisfy the physical requirements of measure preservation (the nonlocal analog of vanishing velocity divergence), continuity (no introduction of discontinuities by the mapping operation), and scale locality (at most order-unity changes in property gradients). The first two requirements are fundamental properties. The requirement of scale locality is based on the principle that length-scale reduction in a turbulent cascade occurs by a sequence of small steps (corresponding to turbulent eddies), causing down-scale energy transfer to be effectively local in wavenumber.

Mathematically, the triplet map is defined as

$$f(y) \equiv y_0 + \begin{cases} 3(y-y_0) & \text{if } y_0 \leqslant y \leqslant y_0 + (1/3)l, \\ 2l - 3(y-y_0) & \text{if } y_0 + (1/3)l \leqslant y \leqslant y_0 + (2/3)l, \\ 3(y-y_0) - 2l & \text{if } y_0 + (2/3)l \leqslant y \leqslant y_0 + l, \\ y - y_0 & \text{otherwise.} \end{cases} \tag{9}$$

This mapping takes a line segment $[y_0, y_0 + l]$, shrinks it to a third of its original length, and then places three copies on the original domain. The middle copy is reversed, which maintains the continuity of advected fields and introduces the rotational folding effect of turbulent eddy motion. Property fields outside the size-l segment are unaffected.

In Eq. (8), K is a kernel function that is defined as $K(y) = y - f(y)$, i.e., its value is equal to the distance the local fluid element is displaced. It is non-zero only within the eddy interval, and it integrates to zero so that the process does not change the total (y-integrated) momentum of individual velocity components. It provides a mechanism for energy redistribution among velocity components, an important characteristic that enables the model to simulate the tendency of turbulent eddies to drive the flow toward isotropy.

The kinetic energy of an individual velocity component i is

$$E_i \equiv \frac{1}{2}\rho \int v_i^2(y)\,\mathrm{d}y. \tag{10}$$

(The density ρ, assumed constant, is defined here as mass per unit length.) The amplitudes c_i in Eq. (8) are determined for each eddy individually subject to the following constraints: (1) the total kinetic energy $E \equiv \sum_i E_i$ remains constant, and (2) the energy removed from any individual velocity component by the kernel mechanism cannot exceed the energy available for extraction (see [27] for details). The values of c_i are governed by the relation

$$c_i = \frac{27}{4l}\left(-v_{i,K} + \mathrm{sgn}(v_{i,K})\sqrt{(1-\alpha)v_{i,K}^2 + \frac{\alpha}{2}\sum_{j\neq i} v_{j,K}^2}\right), \tag{11}$$

where

$$v_{i,K} \equiv \frac{1}{l^2}\int v_i(f(y))K(y)\,\mathrm{d}y = \frac{4}{9l^2}\int_{y_0}^{y_0+l} v_i(y)[l-2(y-y_0)]\,\mathrm{d}y \tag{12}$$

and the degree of energy redistribution is parameterized by an energy transfer coefficient α. The value $\alpha = 2/3$ corresponds to equipartition of the available energy among velocity components and is used to obtain the results presented here. Kerstein et al. [27] consider the effect of setting $\alpha = 1$, which maximizes the intercomponent energy transfer. Although this choice has an impact on some velocity statistics, it is found that properties of interest here are not very sensitive to the choice of α.

2.2. Eddy selection

The final ingredient required in the model is the determination of the time sequence of eddy events, individually parameterized by position y_0 and size l, that are implemented. In ODT, eddy events are implemented instantaneously, but must occur with frequencies comparable to the turnover frequencies of corresponding turbulent eddies. Events are therefore determined by sampling from an event-rate distribution that reflects the physics governing eddy turnovers. A key feature of this distribution is that it is based on the instantaneous state of the flow, and thus evolves in time as the flow evolves.

At each instant in time, the event-rate distribution is defined by first associating a time scale $\tau(y_0, l)$ with every possible eddy event. To this end, the quantity l/τ is interpreted as an eddy velocity and $\rho l^3/\tau^2$ is interpreted as a measure of the energy of eddy motion. To determine τ, this energy is equated to an appropriate measure of the eddy energy based on the current flow state. For reasons explained elsewhere [27], the energy measure that is used is the available energy of the $i = 2$ velocity component upon completion of eddy implementation, minus an energy penalty that reflects viscous dissipation effects. The energy penalty introduces a threshold Reynolds number that must be exceeded for eddy turnover to be allowable.

Based on these considerations, we use the relationship

$$\left(\frac{l}{\tau}\right)^2 \sim (1-\alpha)v_{2,K}^2 + \frac{\alpha}{2}(v_{1,K}^2 + v_{3,K}^2) - Z\frac{\nu^2}{l^2} \tag{13}$$

to determine τ, where the coefficient Z in the viscous penalty is an order-unity parameter of the model.

Given Eq. (13), the time scales τ for all possible eddies can be translated into an event-rate distribution λ, defined as

$$\lambda(y_0, l; t) \equiv \frac{C}{l^2 \tau(y_0, l; t)} = \frac{Cv}{l^4} \sqrt{(1-\alpha)\left(\frac{v_{2,K} l}{v}\right)^2 + \frac{\alpha}{2}\left[\left(\frac{v_{1,K} l}{v}\right)^2 + \left(\frac{v_{3,K} l}{v}\right)^2\right]} - Z, \tag{14}$$

where C is an adjustable parameter that controls the overall event frequency. If the right-hand side of Eq. (13) is negative, the eddy is deemed to be suppressed by viscous damping and λ is taken to be zero for that case. In the square root term of Eq. (14), the quantities preceding Z involve groups that have the form of a Reynolds number. Z can be viewed in this context as a parameter controlling the threshold Reynolds number for eddy turnover.

The foregoing construction of the event-rate distribution involves three free parameters: C, α, and Z. The overall rate constant C determines the relative strength of the turbulent stirring in the model. The transfer coefficient α determines the degree of kinetic energy exchange among velocity components. The viscous cutoff parameter Z determines the smallest eddy size for given local strain conditions. What remains in order to completely specify an ODT flow simulation are the physical properties of the fluid (density, viscosity, etc.) and the proper definition of initial and boundary conditions. Of these, only the boundary conditions for confined turbulent flows require further discussion here.

The boundary condition for molecular evolution, Eq. (6), is simply the standard no-slip condition, i.e., the velocity components are set equal to the wall values. In confined flows, the turbulent stirring model also feels the effect of boundaries through the implicit limitation they place on where eddies can occur and their maximum length scale, $L_{\max}$. For example, in an ODT simulation of turbulent channel flow, the largest mathematically realizable eddy event is equal to the channel width. However, since an eddy event is simply a model for turbulent mixing, it should not be surprising that the behavior of real 3D flow is better represented by setting $L_{\max}$ to a somewhat smaller value. Although not significant in the LES/ODT submodel introduced here (where the LES/ODT coupling limits the physical size of the maximum eddy length), this interesting detail is illustrated in example calculations of channel flow using stand-alone ODT in Section 2.4.

Finally, we briefly note that an additional step is typically introduced in stand-alone calculations in order to suppress unphysically large eddies that may otherwise occasionally occur. Like other multiscale models, ODT has a low-wavenumber divergence that must be suppressed by introducing a cutoff mechanism [25]. For the example stand-alone calculations presented below, the 'median method' described in [27] is used. However, this detail is also unimportant to the LES/ODT coupling developed here because in this context the ODT eddy event size is restricted, by construction, to only those length scales unresolved by the LES.

2.3. Numerical implementation

Neglecting data-gathering procedures, the numerical implementation of an ODT simulation involves three subprocesses: molecular evolution, eddy selection, and eddy implementation.

Molecular evolution according to Eq. (6) can be computed numerically using any conventional approach. In the calculations performed here the molecular evolution is computed each time the eddy event-rate distribution is sampled, leading to very small time steps. Therefore first-order explicit time integration coupled with second-order central differencing of the diffusion term is employed.

As explained above, the sequence of eddy events implemented during a simulated realization is determined by sampling from the rate distribution λ. However, each event, as well as the viscous evolution, Eq. (6), between events, changes the velocity profiles v_i and therefore modifies the rate distribution. From a computational viewpoint this is a problem because it causes explicit construction of, and sampling from, the rate distribution to be unaffordable owing to the need to repeatedly reconstruct this distribution.

To overcome this problem an indirect, but mathematically equivalent, procedure is employed that is analogous to the 'rejection method' described by Ross [40, p. 63], and is implemented once per eddy time

step Δt_{eddy}. In this procedure a candidate eddy is chosen by random sampling of y_0 and l values from a joint probability density function $g(y_0, l; t)$, called the trial PDF. In principle, the trial PDF can be almost arbitrary (it is subject to some weak constraints), though the procedure is most efficient if it approximates the true distribution. The remainder of the procedure is a determination of whether or not this candidate eddy should be implemented.

The implementation decision is based on the model (described in Section 2.2) that determines the 'turnover time' τ for the chosen eddy based on the instantaneous state of the simulated flow (for present purposes, the v_i profiles). τ is used to determine a physically based value of the probability density of the sampled values of y_0 and l. By comparing this probability density and the probability density given by the trial PDF $g(y_0, l; t)$ used for sampling, an acceptance probability P_{a} is computed that has a value between zero and one. The final step is simply to accept the event probabilistically at a rate equal to this acceptance probability.

The event statistics resulting from the combined process of sampling and subsequent acceptance or rejection of a candidate eddy closely approximate the event statistics specified by the physical model. The indirect procedure reproduces the statistics of the direct procedure to any desired accuracy by choosing a small enough sampling time step Δt_{eddy}.

As further explanation we note that $\lambda(y_0, l; t)$ can be viewed as the product of an overall rate of eddy events, $R = \int \lambda(y_0, l; t)\,\mathrm{d}y_0\,\mathrm{d}l$, and a probability density function, $R^{-1}\lambda(y_0, l; t)$, from which eddy parameters y_0 and l are sampled. On this basis, the probability of acceptance of a candidate eddy P_{a} is the product of $R\Delta t_{\text{eddy}}$ (the ratio of the model-prescribed event-rate and the numerically implemented eddy-sampling rate) and $\lambda(y_0, l; t)/[Rg(y_0, l; t)]$ (the ratio of the model-prescribed probability density of the sampled parameter values and the probability density according to the trial PDF $g(y_0, l; t)$ that is sampled to select the parameters of the candidate eddy). $R\Delta t_{\text{eddy}} \ll 1$ is a necessary condition for the select-and-decide procedure to approximate closely the eddy statistics that would be obtained by direct random sampling of the rate distribution $\lambda(y_0, l; t)$ [25].

Eddy implementation on a discretized domain requires the definition of the discrete eddy event. For conservative implementation, the discrete triplet map is defined as a permutation of the cells of the discrete domain. The eddy interval is taken to be an integer multiple of three cells. The smallest consistently defined permutation involves six cells. Continuous and discrete representations of the triplet map are illustrated in Figs. 2(a) and (b) respectively. In Fig. 2(c) the discrete implementation of Eq. (8), including the kernel function, on a three-component velocity field is illustrated. For this example, the initial values of v and w are uniform, but u has a linear profile. This highlights the transfer of kinetic energy among velocity components using the kernel function.

2.4. Stand-alone ODT simulations of channel flow

The application of ODT as a stand-alone model for turbulent channel flow is demonstrated because it illustrates the method for determining the ODT model constants. This application is also used as an initial benchmark for the coupled LES/ODT model.

Fully developed turbulent flow in a planar channel of width $2h$ is simulated by applying the boundary conditions $v_i = 0$ to all velocity components, and introducing a fixed source term $-(1/\rho)(\partial P/\mathrm{d}x)$ on the right-hand side of Eq. (6) for $i = 1$. This term introduces an imposed mean pressure gradient in the streamwise (x) direction, but does not include pressure fluctuations. (Pressure fluctuations are not modeled explicitly, but their effects are represented in the implementation of eddy events.)

ODT results for statistically steady flow are compared to corresponding DNS results of Moser et al. [33], who report results for $Re_\tau = 180$, 395, and 590. Here, $Re_\tau = u_\tau h/\nu$, where $u_\tau = \sqrt{\nu \mathrm{d}v_1/\mathrm{d}y|_{y=0}}$ is the friction velocity. Grid-independent results were obtained for uniformly discretized meshes with $\Delta y^+ < 1$ ($y^+ = yu_\tau/\nu$).

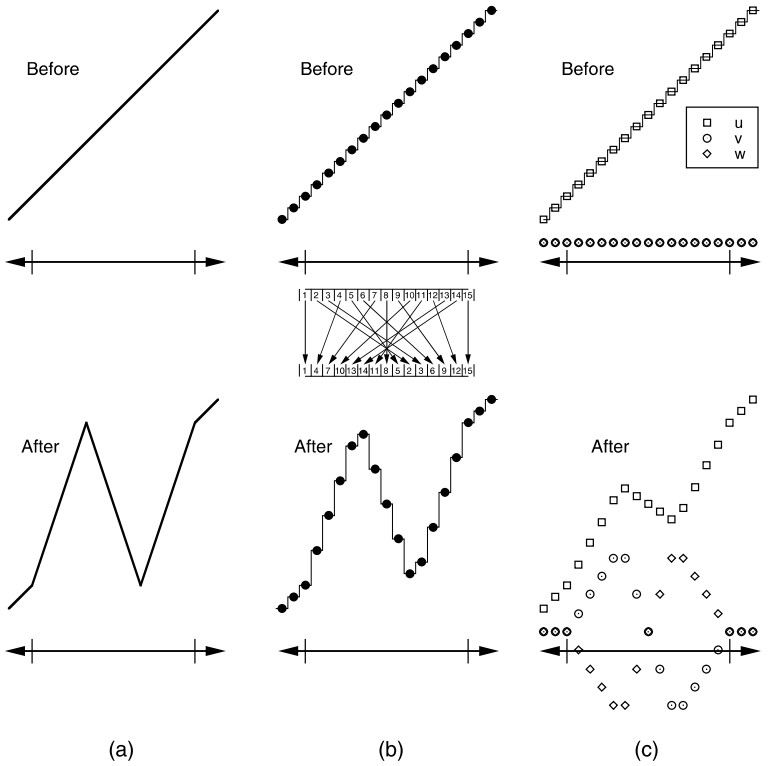

Fig. 2. Illustration of: (a) an analytical triplet map of a scalar with initially uniform gradient, (b) a discrete triplet map of a scalar with initially uniform gradient, and (c) a discrete eddy event on a three-component ODT velocity field where the initial values of v and w are uniformly zero.

To perform the simulations, values of C, Z, α and $L_{\max}$ must be specified. The friction law is sensitive mainly to C, which controls the turbulence intensity. By controlling the frequency of small eddies (i.e., the viscous cutoff), Z mainly affects the transition of the mean velocity profile from the near-wall viscous sublayer to the log-law region, thus defining the nature of the buffer layer. The effect of neglecting Z (by setting Z to a very small value) is illustrated by curve (a) in Fig. 3. For this case, adjustment of C to obtain a good fit to the friction law yields a value $C = 6.22$ and a mean velocity profile in which the buffer layer is essentially removed and the log layer extends down to within numerical resolution of the wall.

Optimum values of C and Z were found by adjusting these parameters to obtain a good match to the DNS friction coefficient and mean velocity profile at $Re_\tau = 590$, while keeping the values of α and $L_{\max}$ constant and equal to $2/3$ (corresponding to an equalization of component energies) and $2h$ (the channel width), respectively. This yields curve (b) of Fig. 3, for which $C = 12.73$ and $Z = 98$. Finally, curve (c) of Fig. 3 illustrates the effect of adjusting the value of $L_{\max}$. For $L_{\max} = 2h$, the wake region of the flow (the flow in the central portion of the channel) is not well represented. However, for $L_{\max} = h$, the wake region is captured quite well.

Based on these results the best-fit values for the ODT model parameters are taken to be $C = 12.73$, $Z = 98$, and $L_{\max} = h$, and are held constant for simulations at all other Reynolds numbers.

Fig. 4 shows computed friction coefficients over a range of Reynolds numbers and compares ODT values with the DNS data of Moser et al. [33] and the turbulent correlation of Dean [12]. The Reynolds number used in this plot is based on the bulk velocity $\bar{U}$ and the channel width $2h$, and the friction coefficient is

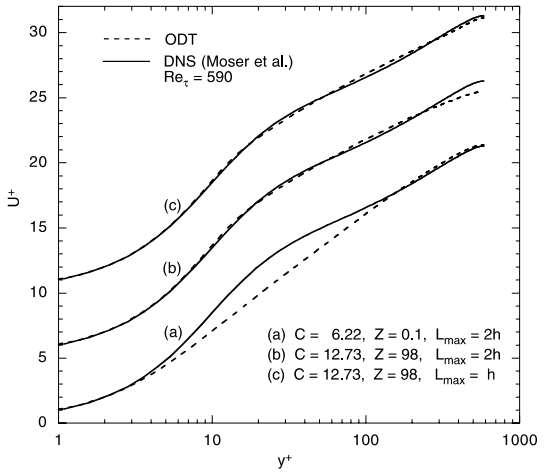

Fig. 3. Semilog plot of ODT and DNS [33] mean velocity profiles for channel flow at $Re_\tau = 590$, in wall coordinates. Note that (b) and (c) are vertically offset from (a) for clarity in illustrating the effects of changing the ODT model parameters.

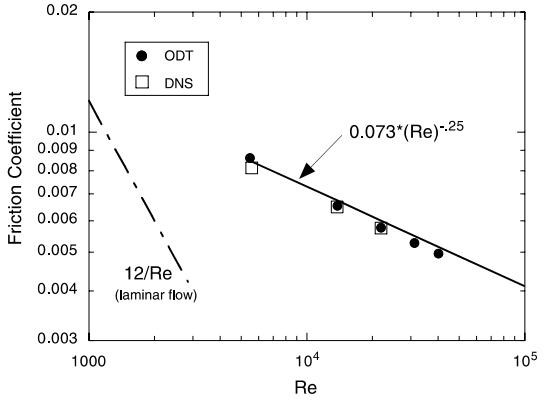

Fig. 4. ODT computed friction coefficient C_f for channel flow compared to DNS data [33] and the correlation of Dean [12]. Here, Re is based on the bulk velocity and the channel width ($2h$).

defined as $C_f = 2(u_\tau/\bar{U})^2$. Good agreement is obtained with the DNS C_f value at $Re_\tau = 395$ but a slight overprediction of C_f at $Re_\tau = 180$ is observed. ODT is formulated based on scalings applicable to high-intensity turbulence, so it may provide a less accurate representation of the weak turbulence at this Re_τ value. For the other flow properties considered here, neither DNS nor ODT exhibit much sensitivity to Re_τ, so additional stand-alone results are shown only for $Re_\tau = 590$.

Although ODT is only 1D in space, transient velocity fluctuations are fully resolved in time, and higher order statistical quantities of interest can be computed. For example, the diagonal components, and the nonvanishing off-diagonal component, of the scaled Reynolds-stress tensor for turbulent channel flow are shown in Fig. 5 and compared to DNS data. The physically valid ODT definitions of these and other high-order statistics are explained in detail elsewhere [25,27]. Of note is that $\langle v_1' v_2' \rangle$ compares very well, but the diagonal components are somewhat underpredicted by ODT. We also see a small dip at the near-wall peak of the streamwise component of the Reynolds stress – an artifact that is due to the combined effects of ODT

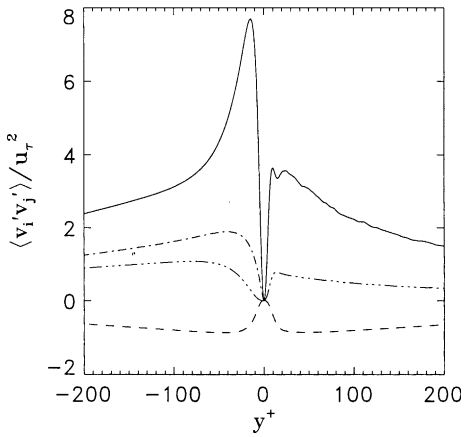

Fig. 5. Lateral profiles of Reynolds stress components in channel flow, scaled by u_τ^2: (—) $\langle v_1'^2\rangle$; (–···–) $\langle v_2'^2\rangle$; (– · –) $\langle v_3'^2\rangle$; (– – –) $\langle v_1'v_2'\rangle$. (The ODT $\langle v_3'^2\rangle$ profile is identical to the ODT $\langle v_2'^2\rangle$ profile.) ODT and DNS [33] results are plotted right and left of centerline, respectively.

eddy structure (see Fig. 2) and near-wall eddy statistics. Later it is shown that coupled LES/ODT results for the diagonal components are in much better agreement with DNS results, suggesting a more realistic forcing of the near-wall region when the bulk flow is modeled with LES and the effects are coupled to ODT. Fig. 5 also illustrates that $\langle v_2'^2\rangle$ and $\langle v_3'^2\rangle$ are statistically identical in the current ODT model. This is due to the coordinate invariance of the pressure scrambling mechanism used in the present multi-component formulation. More general formulations that break this symmetry (and involve three distinct eddy types) have been tested, but are not applied here.

In another illustration shown in Fig. 6, remarkable similarity is shown between ODT and DNS for different terms of the v_1 variance budget. Although some differences are seen, the results suggest that despite being a 1D model, the near-wall flow energetics of ODT reflect fundamental characteristics of 3D turbulent flow.

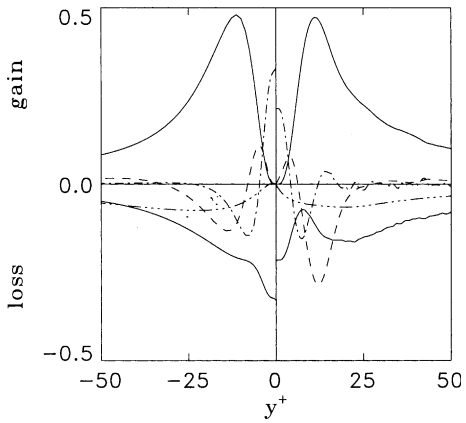

Fig. 6. Budget of $\langle v_1'^2\rangle$ in channel flow, in wall coordinates: (—) production (upper), dissipation (lower); (– – –) advective transport; (– · –) viscous transport; (–···–) scrambling. ODT and DNS [33] results are plotted right and left of centerline, respectively.

3. Summary of the LES bulk-flow model

In the current approach, turbulent flow away from the wall (i.e., the bulk flow) can be modeled by any standard LES approach. Here we briefly review the LES equations and the dynamic Smagorinsky subgrid model used in the present work.

The classic LES equations are well known (e.g., see [11,18,41]), and can be derived by applying the concept of spatial filtering to the continuity and Navier–Stokes equations. Assuming the filter commutes with differentiation, and for an incompressible fluid with constant properties, the following LES equations of motion can be derived:

$$\rho\frac{\partial\bar{u}_i}{\partial t}+\rho\frac{\partial}{\partial x_j}(\overline{u_iu_j})=-\frac{\partial\bar{p}}{\partial x_i}+\frac{\partial}{\partial x_j}\left[\mu\left(\frac{\partial\bar{u}_i}{\partial x_j}\right)\right]+\rho\bar{f}_i, \tag{15}$$

$$\frac{\partial\bar{u}_i}{\partial x_i}=0. \tag{16}$$

Here, $\mu=\rho\nu$ is the dynamic viscosity and the spatial coordinates are denoted (x_1,x_2,x_3) instead of (x,y,z) to allow use of the convention that repeated indices imply summation (unless stated otherwise). These two notations are used interchangeably in what follows because each is more convenient in certain contexts. Also, u rather than v is used to denoted velocity. Throughout the paper, u is used in LES equations and v is used in equations governing ODT processes so that the origin (LES or ODT) of quantities appearing in the combined LES/ODT formulation is clear in all instances.

To solve the LES equations a closure model must be chosen for the nonlinear advective term (the second term in Eq. (15)). To this end, it is common to define a subgrid-scale stress tensor as follows:

$$\tau_{ij}=\overline{u_iu_j}-\bar{u}_i\bar{u}_j. \tag{17}$$

Gradient-diffusion models adopt the hypothesis that the anisotropic part of the subgrid-scale stress tensor τ is proportional to the resolved (large scale) strain-rate tensor $\mathbf{S}$:

$$\tau_{ij}-\frac{1}{3}\delta_{ij}\tau_{kk}=-2\frac{\mu_S}{\rho}\bar{\mathbf{S}}_{ij}, \tag{18}$$

$$\bar{\mathbf{S}}_{ij}=\frac{1}{2}\left(\frac{\partial\bar{u}_i}{\partial x_j}+\frac{\partial\bar{u}_j}{\partial x_i}\right), \tag{19}$$

where μ_S is a subgrid eddy viscosity, which must be computed from an appropriate model, and δ_{ij} is the Kronecker delta. By defining a modified pressure $\bar{P}$ that includes the subgrid kinetic energy (i.e., the trace of τ), and dropping the body-force term $\rho\bar{f}_i$ for simplicity, Eq. (15) can now be expressed as

$$\rho\frac{\partial\bar{u}_i}{\partial t}+\rho\frac{\partial}{\partial x_j}(\bar{u}_i\bar{u}_j)=-\frac{\partial\bar{P}}{\partial x_i}+\frac{\partial}{\partial x_j}\left[(\mu+\mu_S)\left(\frac{\partial\bar{u}_i}{\partial x_j}\right)\right]. \tag{20}$$

One of the first models for the subgrid eddy viscosity was introduced by Smagorinsky [43] and it remains, together with its variants, a widely applied model. It can be written compactly as

$$\mu_S=\rho(C_S\Delta)^2(2\bar{\mathbf{S}}_{ij}\bar{\mathbf{S}}_{ij})^{1/2}, \tag{21}$$

where C_S is called the Smagorinsky coefficient, and the characteristic filter width Δ is generally computed as the cube root of the local cell volume:

$$\Delta = (\Delta x_1 \Delta x_2 \Delta x_3)^{1/3}. \tag{22}$$

A method for dynamically adjusting the Smagorinsky coefficient to the local features of the flow was first suggested by Germano et al. [16]. The basic idea is to assume that the constant in the eddy-viscosity relationship is the same for a second filter of larger width Δ'. Given this second filter, typically referred to as the test filter, we can define a second subgrid-scale stress tensor $\mathbf{T}_{ij}$ as follows:

$$\mathbf{T}_{ij} = \widetilde{\widetilde{u_i u_j}} - \tilde{\tilde{u}}_i \tilde{\tilde{u}}_j. \tag{23}$$

The tilde denotes the test filter, here applied to quantities that have already been subject to a filter of width Δ. We now note that the difference between this tensor $\mathbf{T}_{ij}$ and the filtered value of τ_{ij} (using the test filter) can be written in terms of quantities that can be computed, i.e.,

$$\mathbf{L}_{ij} = \mathbf{T}_{ij} - \tilde{\tau}_{ij} = \widetilde{\bar{u}_i \bar{u}_j} - \tilde{\bar{u}}_i \tilde{\bar{u}}_j. \tag{24}$$

If we apply the assumption that the Smagorinsky coefficient is the same at both filter widths, then we can write

$$\widetilde{\bar{u}_i \bar{u}_j} - \tilde{\bar{u}}_i \tilde{\bar{u}}_j = 2(C_S \Delta')^2 |\bar{\mathbf{S}}'| \bar{\mathbf{S}}'_{ij} - 2\widetilde{(C_S \Delta)^2 |\bar{\mathbf{S}}| \bar{\mathbf{S}}_{ij}}, \tag{25}$$

where the wide tilde over the rightmost term indicates test filtering of the entire term. This is an overdetermined but closed system of equations for the Smagorinsky coefficient C_S. The most common method of dealing with the overdeterminancy is to use the least-squares solution described by Lilly [30]. However, the fact that C_S appears inside the filtering operation (second term on the right-hand side of Eq. (25)) introduces some additional mathematical and practical problems for which various solutions have been proposed. These are discussed by Ghosal et al. [17], who propose a dynamic localization procedure which uses a constrained variational formulation.

For flows with two homogeneous directions, such as fully developed turbulent flow between parallel plates, the following formula is obtained by assuming that C_S is only a function of y and t and is positive [17]:

$$C_S(y,t) = \left[\frac{\langle \mathbf{m}_{ij} \mathbf{L}_{ij} \rangle_{xz}}{\langle \mathbf{m}_{kl} \mathbf{m}_{kl} \rangle_{xz}} \right]_+. \tag{26}$$

Here $\mathbf{m}_{ij} = 2(\Delta')^2 |\bar{\mathbf{S}}'| \bar{\mathbf{S}}'_{ij} - 2\widetilde{(\Delta)^2 |\bar{\mathbf{S}}| \bar{\mathbf{S}}_{ij}}$, $\langle \rangle_{xz}$ denotes integration over a layer of finite thickness in the xz plane, and the brackets with a $+$ subscript denote the operation of taking the positive part, i.e., $[x]_+ = \frac{1}{2}(x + |x|)$ for any real number x.

The dynamic Smagorinsky subgrid model just described completes the description of the bulk-flow LES model used in this work. In practice, discrete approximate forms of these equations are solved using the second-order numerical method described later in Section 4.5.

An alternative, conceptually distinct way to develop the discrete LES equations is described by Schumann [42]. This approach is important to note here because it is invoked in the ODT-based near-wall model described below. Called the 'volume-balance method,' the averaged quantities correspond to a discrete number of volumes that are fixed in space (i.e., the mesh). In essence, it is simply a control-volume numerical scheme developed for LES. The governing equations are integrated by parts to obtain discrete budget equations for the individual mesh cells. The modeling problem then reduces to representing the unresolved surface fluxes in terms of the spatially averaged quantities that are available, and similar

methods as described above can be used to develop closure models. An advantage of this method is that irregular or anisotropic meshes do not introduce fundamental errors. (For the classic approach with non-uniform meshes, filter commutativity becomes a problem [41].) Adopting Schumann's notation, the discrete momentum equation that would correspond to Eq. (15) above can be written as

$$\rho \frac{\partial \bar{u}_i}{\partial t} + \rho \delta_j (\overline{u_i u_j}^{\mathrm{S}}) = -\delta_i \bar{p} + \delta_j \left[\mu \left(\overline{\frac{\partial u_i}{\partial x_j}}^{\mathrm{S}} \right) \right] + \rho \bar{f}_i, \tag{27}$$

where δ denotes a numerical-difference operator, and the advective and diffusive flux terms are averages over surfaces, not volume averages.

4. Formulation of an ODT-based near-wall subgrid model

Having summarized both the ODT stand-alone model and the LES model, we now describe a method for coupling the highly resolved (in 1D space) ODT model, near all no-slip walls, with traditional 3D LES turbulence modeling in the bulk flow.

4.1. Geometric considerations

The ODT wall model affects the LES equations in the two distinct near-wall regions illustrated in Fig. 1(c). For reference purposes, we call the layer of LES cells that are immediately adjacent to the no-slip wall the ODT inner region. It is in this region that the ODT model is primarily active. Although the ODT evolution equations (Section 4.2) are only solved in the inner region, eddy events can extend from any location within the inner region out into the LES domain. Therefore a second region, called the LES/ODT overlap region, extends outward from the top of the inner region through a number of additional LES cell layers. The extent of this region is determined by the length of the largest allowable eddy event, $L_{\max}$, which in this context is related to the LES filter width. The flow in the overlap region is primarily controlled by standard LES equations, but is affected by eddy events through an LES/ODT coupling described in Section 4.3.

Within each inner-region LES control volume, we define an ODT line that begins at the no-slip wall and extends upward to the top of the control volume. For reasons described below, an ODT sub-control volume is also defined and associated with each mesh point on the ODT line, as illustrated in Fig. 7. All three ODT velocity components as well as any scalar quantities of interest, except pressure, are spatially resolved in the wall-normal direction on the ODT lines. Pressure is only resolved on the LES-scale mesh (i.e., one value per LES control volume) because 3D continuity constraints are imposed by pressure only on the LES grid.

4.2. Revised ODT evolution equations

As a stand-alone model, ODT is a closed system that consists of a single ODT line. When associated with a fixed spatial location, this form of the ODT model is applicable to flows where turbulent flow properties are invariant in directions perpendicular to the ODT line. These conditions are not met in the present application where the near-wall region consists of a forest of ODT lines (each associated with an LES control volume) which, in general, may see spatially varying flow conditions. Therefore a revised form of the ODT model is needed for use as an LES wall model. In the present approach this is accomplished by modifying the ODT evolution equations (see Eq. (6)) as follows:

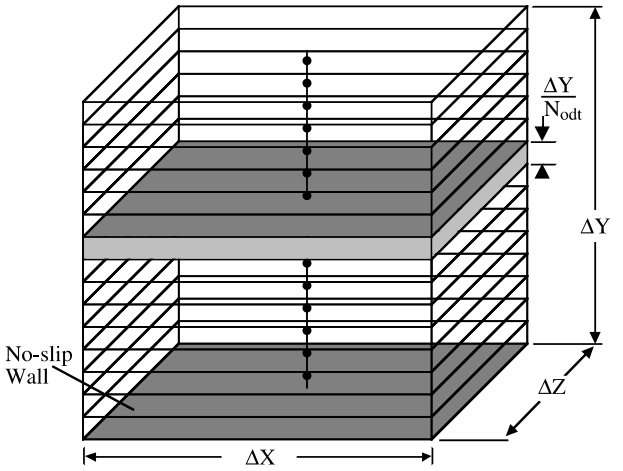

Fig. 7. Illustration of ODT points and sub-control volumes embedded in an 'inner-region' LES control volume. The nominal ODT domain is the wall-normal line passing through the center of the control volume. Points of the discretized domain also mark the ODT sub-control volumes.

$$\left(\partial_t - \nu\partial_{x_2}^2\right) v_i(y,t) + \partial_{x_j}\left(V_j(y,t)v_i(y,t)\right) + \frac{1}{\rho}\frac{\partial \bar{P}}{\partial x_i}\bigg|_{i\neq 2} = 0. \tag{28}$$

Here, advective transfer terms due to a local advective velocity field $V_j(y,t)$ have been introduced, and an LES-scale pressure gradient term (assumed constant between LES time steps) has been included except in the wall-normal direction ($i = 2$). These equations can be viewed as expressions of ODT momentum conservation over the sub-control volumes illustrated in Fig. 7, and have a form that is similar to the thin boundary-layer equations used in the two-layer wall model of Balaras et al. [4,5] (see Eq. (4)). In the present model the $j = 1$ and $j = 3$ components of the advective velocity field are defined as a time-average of the ODT velocities,

$$V_j(y,t) = \frac{1}{\Delta t}\int_{t-\Delta t}^{t} v_j(y,t')\,\mathrm{d}t', \quad j \neq 2, \tag{29}$$

where the temporal filter size has been defined as the LES time step Δt.

The additional terms added to the ODT evolution equation involve the pressure gradient and the specially defined 'advecting' velocity. Both of these are quantities that have a temporal variation that occurs over LES time scales, not ODT time scales. Thus the shorter time scale nature of the ODT fluctuations is largely unaffected, but longer time scale effects can still be felt.

There is an important distinction between the instantaneous wall-normal ODT velocity component v_2 and the instantaneous tangential velocity components v_1 and v_3. In the approach developed here, v_1 and v_3 are treated as having an advecting quality in that we compute V_1 and V_3 from them. However, v_2 is treated differently because eddy events are the model for turbulent transport in the wall-normal direction. We conceptualize v_2 as simply a representation of the wall-normal velocity component kinetic energy per unit mass (actually the square root of that energy). Thus, no pressure gradient is included in the evolution equation for v_2. To compute the advective transport velocity in the wall-normal direction, V_2, we simply apply continuity and integrate from the wall, as follows:

$$V_2(y,t) = -\int_0^y \left(\frac{\partial V_1}{\partial x_1} + \frac{\partial V_3}{\partial x_3} \right) \mathrm{d}y. \tag{30}$$

Note that this method to compute a wall-normal velocity is also used in the two-layer wall-stress model [5,9] discussed in Section 1 (see Eq. (5)) and that this automatically satisfies continuity within the LES-scale control volume.

Modeling the advection terms with velocities that involve temporal filtering of v_1 and v_3 is justified because the spatial derivatives in the $i = 1$ and $i = 3$ directions in Eq. (28) are implemented numerically as spatial differences over LES-scale spatial increments ΔX and ΔZ, respectively, as illustrated by the LES/ODT control-volume geometry sketched in Fig. 7. (Thus, all functions of y in Eq. (28) are also functions of x and z, though these dependencies are not shown explicitly.) In view of the coarseness of the x and z resolution relative to the y resolution, the convective time scale for property transfer between laterally adjacent ODT sub-volumes is the LES time scale Δt rather than the fine-grained time scale on which other ODT processes evolve. Accordingly, temporal filtering suppresses unphysical high-frequency fluctuations due to the more rapid evolution processes implemented in the vertical direction (which can be resolved temporally owing to the finer spatial resolution in that direction). Of note is that the limit of the temporal filter size going to infinity corresponds to the limit of ΔX and ΔZ going to infinity, in which case the advective term goes to zero and the equations reduce to the stand-alone ODT equations for channel flow discussed in Section 2.

The ODT evolution equations are solved only in the inner region and boundary conditions must be applied both at the wall ($y = 0$) and at the top of the inner region ($y = \Delta Y$). At $y = \Delta Y$ this is accomplished by assuming a linear variation of all velocity components at every instant in time between the last ODT node ($y = \Delta Y$) and the corresponding LES values in the overlap region at $y = \frac{3}{2}\Delta Y$. (The LES grid structure and its implications for LES/ODT coupling are discussed in Section 4.6.) Given this assumption, all required boundary fluxes (both advective and diffusive) can be computed based on the boundary conditions at $y = 0$:

$$\begin{aligned} &v_1 = v_2 = v_3 = 0, \\ &V_2 = 0 \end{aligned} \tag{31}$$

and at $y = \Delta Y$:

$$\frac{\partial v_i}{\partial x_2} = \left(\bar{\boldsymbol{u}}_i|_{y=(3/2)\Delta Y} - v_i|_{y=\Delta Y} \right) / [\Delta Y/2]. \tag{32}$$

Note that in Eq. (32), $\bar{\boldsymbol{u}}_i|_{y=(3/2)\Delta Y}$ denotes the current value of LES velocity component i at a distance from the wall equal to $\frac{3}{2}\Delta Y$.

Although the ODT evolution equations are solved only in the inner region, eddy events can extend from any location within the inner region out into the LES domain.

4.3. LES/ODT coupling

The ODT wall model and the LES bulk flow model are coupled in two different ways. The first is through the boundary conditions that each model sees at the interface region between the two domains. The second relates to the bi-directional influence that solving the LES-scale continuity equation has on each model.

From a boundary condition standpoint, ODT and LES interact in the following way. LES provides ODT with the LES-scale velocities needed as boundary conditions to evolve Eq. (28), and also with the overlap-region velocities required to evaluate and perform eddy events that extend into the overlap region.

Because overlap-region LES control volumes do not contain ODT substructure, linear interpolation of the LES-scale variables in the overlap region is used to provide ODT-resolved values as needed. In addition, because the ODT equations are evolved at very short time scales relative to LES, LES-scale time-averaged fluxes can be computed by summing the momentum transport between near-wall LES control volumes due to ODT processes. ODT thereby provides LES with a complete description of the momentum flux at the the top of the inner region, as well as augmented fluxes at LES control volume interfaces through which any large ODT eddy events have extended. Thus each model provides the other with the information needed to perform their respective simulations. Although conceptually simple, there are several important details which require explanation.

In stand-alone ODT, the length scale of the largest possible eddy event, $L_{\max}$, corresponds to the integral scale of the flow problem. For example, in channel flow the largest possible eddy is physically limited by the distance between the two walls. However, as an LES subgrid model ODT is only intended to model the effects of unresolved small-scale eddies. Therefore, the largest length scales modeled by ODT, $L_{\max}$, should correspond to the smallest length scales captured by the LES. Fig. 8 illustrates that eddies can therefore extend out as far as $y = \Delta Y + L_{\max}$, which defines the boundary of the overlap region. The details of how we determine the value of $L_{\max}$ are discussed in Section 5.

From an LES perspective, the main role of the ODT wall model is to provide the contribution of subgrid-scale processes to momentum fluxes between near-wall LES control volumes. The determination of these fluxes involves, at the ODT level, specification of the areas of control surfaces across which momentum is fluxed, both by eddy events and by viscous evolution within ODT. This is one of several motivations for the introduction of the sub-control-volume interpretation of ODT (Fig. 7). However, in this context the distinction between, and the respective roles of, the point value (i.e., line-of-sight) and control-volume interpretations of ODT evolution processes require careful consideration.

As described in Section 2, ODT is formulated so that the eddy-event distribution emulates the statistics due to 3D eddy motions that might be measured along a representative line of sight. The validity and limitations of the use of this formulation to determine fluxes through control surfaces are examined.

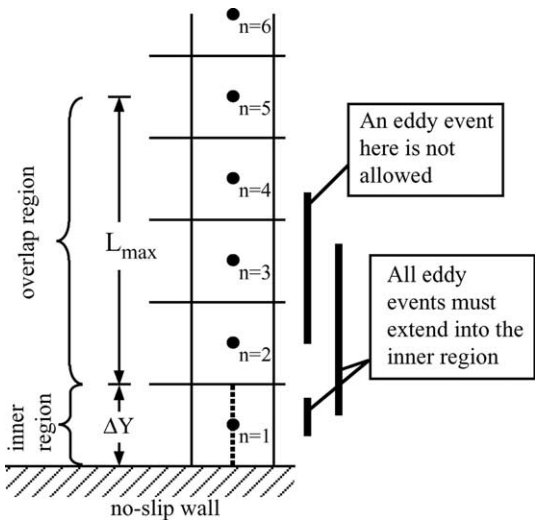

Fig. 8. Illustration of allowable eddy event locations within the near-wall region. The dashed line in the inner region indicates that the fine grained ODT domain exists only in this region.

Consider an ODT line that intersects an orthogonal control surface corresponding to an LES control-volume face. A size-l eddy event can be viewed as the intersection of an eddy of volume l^3 with the ODT domain. If the size-l interval intersects the control surface, then it contributes to property fluxes (e.g., fluxes of velocity components) across that surface. However, the subregion of the control surface that is subject to these fluxes is of order l^2, which can be considerably larger or smaller than the nominal control-surface area. (It can be larger because eddies extending into the overlap region can be larger than the LES mesh spacing.)

Nevertheless, fluxes deduced by assuming that the property transfers associated with any size-l ODT eddy occur across the nominal control-surface area are valid (subject to a caveat) for the following reason. Although the particular eddy transfers properties only across an order-l^2 subregion, these property transfers are representative of transfers across comparably sized subregions everywhere on the control surface. Replicates of the ODT domain arranged in a 2D array with spacing l between neighboring replicates would each induce property transfers analogous to the effects of size-l eddies on the original domain. Note that this reasoning only applies to a particular l value, so this is a conceptual rather than a realizable analogy. Nevertheless, it makes the point that ODT, though formulated from a line-of-sight perspective, is consistent with the LES/ODT control-volume framework.

A caveat in this regard is suggested by further consideration of the conceptual 2D array, with neighbor spacing l, of ODT domains (here taking l to be smaller than the LES mesh spacing). In LES/ODT, one member of this array represents the entire array. This representation is valid on average, but it leads to artificially large property-transfer fluctuations. This representation is equivalent to assuming that the evolution is the same on all members of the array, neglecting statistical differences between processes on individual domains that tend to reduce the aggregate variability of the flux time history across the nominal control surface. Neglect of this effect should not have a major impact on output statistics because the main contribution to property fluxes is from eddy events whose size l is of the order of the LES mesh spacing. Thus, the line-of-sight (or point value) and control-volume interpretations of ODT are not equivalent, but the differences between them are not crucial.

The accumulated fluxes due to eddy events that transfer fluid across LES control-volume interfaces are incorporated into the LES time-stepping scheme, both to enforce consistency between ODT and LES evolution and to evaluate unclosed terms in the LES evolution equations (with details provided in Section 4.6.2). Note that the LES-scale properties at the LES node points are considered unchanged during the fine-grained ODT time evolution. LES-scale effects of ODT processes are implemented during time advancement of the LES equations.

The second mechanism by which LES and ODT couple is through the enforcement of the global LES continuity equation. For this purpose a relationship must be defined between ODT point values and the LES-scale filtered velocities associated with the LES bulk-flow model. To model an LES-filtered velocity $\bar{u}_i$ knowing only the time evolution of a discrete set of ODT values $v_i(y_m,t)$, we make the following approximation:

$$\bar{u}_i(t) = \frac{1}{N_{\mathrm{ODT}}} \sum_{m=1}^{N_{\mathrm{ODT}}} V_{i,m}(y_m,t). \tag{33}$$

In this approximation, the temporally filtered velocity $V_i(y_m,t)$ is used as an estimate of the instantaneous volume average over a sub-control volume of height $\Delta Y/N_{\mathrm{ODT}}$ at a nominal distance $y = y_m = ((m-(1/2))/N_{\mathrm{ODT}})\Delta Y$ above the wall, where ΔY is the height of the LES control volume. Knowing each value of $V_i(y_m,t)$ in the control volume, an LES-scale velocity (whose spatial filter is associated with the near-wall control volume) is computed as the simple average of these values. Because the LES momentum equations are not solved in the inner region, this definition provides an important link in the model between the LES equations and the ODT point values that are evolved.

In the present work, a fractional-step based numerical approach is used to temporally integrate the global conservation equations and enforce continuity constraints on the LES velocity field (Section 4.5). Eq. (33) provides the LES/ODT link required to define the LES velocity field within the near-wall region. As explained in detail in Section 4.6, it also provides the defining relationship that must be enforced when the LES velocity field is corrected based on a solution to the discrete Poisson equation. These LES-scale corrections induce adjustments in the ODT velocities and constitute an important LES-to-ODT coupling that contributes significantly to the overall results.

4.4. Synopsis of the coupled LES/ODT model

As modeled here, the equations simulating the turbulent flow are distinct in each of the three flow regions, i.e., the ODT inner region, the LES/ODT overlap region, and the LES core-flow region.

In the ODT inner region, the revised ODT evolution Eq. (28) is solved subject to the boundary conditions given by Eqs. (31) and (32), and the advecting velocities defined in Section 4.2. Eddy events occur at various times and locations, and with various length scales as per the stochastic model described in Section 2. For eddy events that extend into the overlap region, ODT resolved values are obtained by linear interpolation of the LES-scale variables.

When an instantaneous eddy event extending into the overlap region occurs, time-accurate implementation of conservation laws would require all affected LES quantities to be adjusted based on the net transport across each LES control-volume face. However, in practice, the LES equations of motion are solved numerically using time steps that are much larger than those required by the ODT subgrid model. In the current numerical implementation (described in detail in Section 4.6), explicit LES/ODT coupling is accomplished by accumulating the net transfer across each LES control-volume interface (from all processes) during the ODT evolution within an LES time step. The net transfer during this time period is summed and then divided by the LES time step – thus providing surface fluxes for input to the LES equations. At $y = \Delta Y$, ODT provides the entire flux (analogous to the surface flux values called for in Schumann's LES formulation, Eq. (27)). In the LES/ODT overlap region the LES fluxes are supplemented by the transport associated with ODT eddy events.

In the LES/ODT overlap region, the LES equations are solved subject to a flux-matching condition at the LES/ODT interface (i.e., $y = \Delta Y$), and to the supplemental fluxes caused by eddy events that extend across LES cell boundaries in the overlap region. In the LES core-flow region, the LES equations are solved without modification.

LES time advancement yields a revised LES velocity field that reflects the global effects of the pressure field. At this point, ODT velocities in the inner region are adjusted to be consistent with LES. This adjustment event is similar to an ODT eddy event in that it occurs at an instant in time. However, this event only affects the average velocity in the inner region, not the ODT-scale variations. The specific method used here is explained in Section 4.6.4.

4.5. Description of the LES simulation code

The base LES code used for testing the near-wall ODT subgrid model is a structured-grid second-order finite-difference code specifically designed for doing channel flow [32], and was obtained from Stanford University through our collaboration with the Center for Turbulence Research. In this code, periodic boundary conditions are imposed in the streamwise (x) and spanwise (z) directions and the flow is driven by a constant pressure gradient in the streamwise direction. The grid is staggered (see [20,36]) and can be stretched in the wall-normal direction using a hyperbolic-tangent mapping if desired.

A semi-implicit time-integration algorithm is used where the diffusion terms in the wall-normal direction (y) are treated implicitly with the Crank–Nicholson scheme, and a third-order Runge–Kutta scheme (see [44]) is used for all other terms. The fractional-step method of Dukowicz and Dvinsky [14] is used in conjunction with a Van Kan [23] type of pressure term. The corresponding Poisson equation for pressure is solved using a tri-diagonal matrix algorithm in the wall-normal direction and fast Fourier transforms (FFT) in the periodic directions.

The three-step time-advancement scheme used in the base LES code can be written in the following way:

$$\frac{\bar{u}_i^k - \bar{u}_i^{k-1}}{\Delta t} = \alpha_k \mathbf{L}_y(\bar{u}_i^{k-1}) + \beta_k \mathbf{L}_y(\bar{u}_i^k) + (\alpha_k + \beta_k)\mathbf{L}_{xz}(\bar{u}_i^{k-1}) - \gamma_k \mathbf{N}(\bar{u}_i^{k-1}) - \zeta_k \mathbf{N}(\bar{u}_i^{k-2}) - (\alpha_k + \beta_k)\frac{1}{\rho}\frac{\delta \bar{P}^k}{\delta x_i} - (\alpha_k + \beta_k)\frac{PG_i}{\rho}, \tag{34}$$

$$\frac{\delta \bar{u}_i^k}{\delta x_i} = 0, \tag{35}$$

where $k = 1, 2, 3$ denotes the sub-step number, $\bar{u}_i^0$ and $\bar{u}_i^3$ are the LES velocities at the beginning and end of the time step, and PG_i denotes the constant portion of the pressure gradient driving the channel flow (zero for $i = 2$ and 3). In the present implementation, $\delta/\delta x_i$ denotes a second-order central-difference operator and accordingly, $\mathbf{N}(\bar{u}_i)$ represents a second-order finite-difference approximation to the advection terms:

$$\mathbf{N}(\bar{u}_i) = \frac{\delta}{\delta x_j}(\bar{u}_i \bar{u}_j). \tag{36}$$

Two distinct operators for the viscous terms, $\mathbf{L}_{xz}(\bar{u}_i)$ and $\mathbf{L}_y(\bar{u}_i)$, are defined so that the implicit treatment of the wall-normal diffusion terms can be clearly distinguished:

$$\mathbf{L}_{xz}(\bar{u}_i) = \frac{\delta}{\delta x_j}\left[(\nu + \nu_S)\left(\frac{\delta \bar{u}_i}{\delta x_j}\right)\right], \tag{37}$$

$$\mathbf{L}_y(\bar{u}_i) = \frac{\delta}{\delta x_2}\left[(\nu + \nu_S)\left(\frac{\delta \bar{u}_i}{\delta x_2}\right)\right], \tag{38}$$

where the right-hand side of Eq. (37) is summed over $j = 1$ and 3, the relation $\nu = \mu/\rho$ and the definition $\nu_S = \mu_S/\rho$ of the kinematic eddy viscosity have been introduced, and second-order central differencing is again used.

The time-advancement coefficients α_k, β_k, γ_k, and ζ_k, $k = 1, 2, 3$, are constants selected such that third-order accuracy is obtained for the advection term and second-order accuracy for the viscous term. The values of these coefficients are

$$\gamma_1 = 8/15, \quad \gamma_2 = 5/12, \quad \gamma_3 = 3/4,$$
$$\zeta_1 = 0, \quad \zeta_2 = -17/60, \quad \zeta_3 = -5/12,$$
$$\alpha_1 = 4/15, \quad \alpha_2 = 1/15, \quad \alpha_3 = 1/6,$$
$$\beta_1 = 4/15, \quad \beta_2 = 1/15, \quad \beta_3 = 1/6.$$

Because ζ_1 vanishes, Eq. (34) does not require the evaluation of $\bar{u}_i^{k-2}$ for $k = 1$. The effective sub-time-step for this method is $\Delta t_k = (\alpha_k + \beta_k)\Delta t$.

Applying the fractional-step method of Dukowicz and Dvinsky [14] to Eqs. (34) and (35), we obtain

$$\frac{\hat{\bar{u}}_i^k - \bar{u}_i^{k-1}}{\Delta t} = \alpha_k \mathbf{L}_y(\bar{u}_i^{k-1}) + \beta_k \mathbf{L}_y(\hat{\bar{u}}_i^k) + (\alpha_k + \beta_k)\mathbf{L}_{xz}(\bar{u}_i^{k-1}) - \gamma_k \mathbf{N}(\bar{u}_i^{k-1}) - \zeta_k \mathbf{N}(\bar{u}_i^{k-2}) - (\alpha_k + \beta_k)\frac{1}{\rho}\frac{\delta \bar{P}^{k-1}}{\delta x_i} - (\alpha_k + \beta_k)\frac{PG_i}{\rho}, \tag{39}$$

$$\frac{\bar{u}_i^k - \hat{\bar{u}}_i^k}{\Delta t} = -\frac{\delta \phi^k}{\delta x_i}, \tag{40}$$

where ϕ^k and $\bar{P}$ are related by

$$\frac{\delta \phi^k}{\delta x_i} = (\alpha_k + \beta_k)\frac{1}{\rho}\frac{\delta}{\delta x_i}(\bar{P}^k - \bar{P}^{k-1}) - \beta_k \mathbf{L}_y(\bar{u}_i^k - \hat{\bar{u}}_i^k), \tag{41}$$

and the hat symbol placed over a variable denotes an intermediate value. For clarity we note that Eq. (34) can be recovered by solving for $\hat{\bar{u}}_i^k$ in Eq. (40), and then substituting this identity and that of Eq. (41) back into Eq. (39). In practice, the rightmost term in Eq. (41) is neglected, resulting in the 'splitting' error associated with this method.

Solving for $\bar{u}_i^k$ in Eq. (40) and applying the divergence-free constraint, Eq. (35), we obtain the discrete Poisson equation,

$$\frac{1}{\Delta t}\frac{\delta \hat{\bar{u}}_i^k}{\delta x_i} = \frac{\delta^2 \phi^k}{\delta x_i \delta x_i}. \tag{42}$$

To advance from sub-step $k-1$ to k requires the completion of a two-part fractional-step cycle. In the first part, Eq. (39) is solved for $\hat{\bar{u}}_i^k$, the intermediate or interim velocity field. In the second part, Eq. (42) is solved for ϕ^k. Knowing ϕ^k, Eq. (41) is integrated (with the rightmost term omitted) to compute the change in pressure from $k-1$ to k, and Eq. (40) is used to compute the new velocity field, $\bar{u}_i^k$.

The subgrid-scale model used to compute the subgrid eddy viscosity is the dynamic Smagorinsky model of Germano et al. [16] with the least-square technique of Lilly [30] as described in Section 3. Averaging in the spanwise and streamwise directions is used to compute C_S (see Eq. (26)) and filtering is performed in these directions but not in the y direction. The ratio of the test filter width to the grid filter width is taken to be 2.0.

4.6. Numerical implementation of the near-wall model within an LES code

In order for the LES pressure field to couple properly to the ODT velocities, it is important to assure that the spatial locations of the ODT velocity components are consistent with the LES numerical discretization. In the staggered-grid method used in the LES code, the control volumes for mass and momentum are offset from one another such that the velocity components are calculated for the points that lie on the faces of the mass-conservation control volumes. This is illustrated in Fig. 9, where the LES-scale velocities are represented with large arrow heads, and the locations of the associated ODT velocity components are given by the points that lie on the lines shown.

It is also important for the ODT temporal advancement scheme to couple in a consistent way to the LES code. As described above, the LES time-integration scheme used here is a three-step Runga–Kutta method where each step consists of a two-part fractional-step cycle. To use the ODT wall model, we modify this cycle to include two additional parts specific to the near-wall ODT model. In the new part 1, the inner-region ODT equations are evolved and the momentum exchanges at LES interfaces due to the ODT

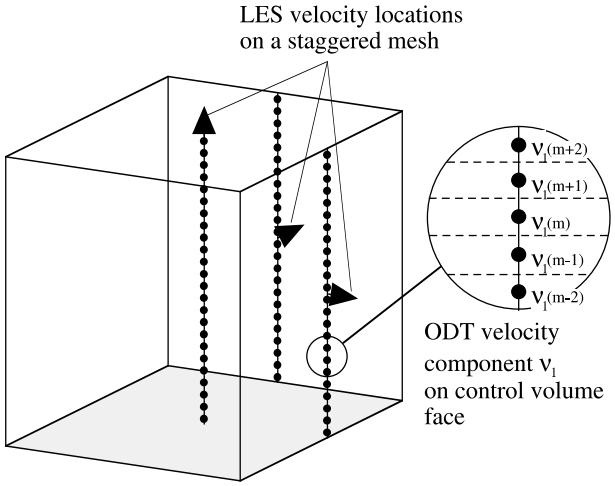

Fig. 9. Spatial location of LES and ODT velocity components on a staggered grid.

processes are summed. At the end of this part, values for interim LES velocities $\hat{\tilde{\boldsymbol{u}}}_i^k$ in the ODT inner region are computed from these results. In part 2, modified forms of Eq. (39) are solved for $\hat{\tilde{\boldsymbol{u}}}_i^k$ throughout the rest of the domain. The modifications correspond to ODT contributions to the surface fluxes in the LES/ODT overlap region. Part 3 is the continuity-enforcing pressure-projection step that involves solving a discrete Poisson equation for a pressure-adjusted velocity field $\bar{\boldsymbol{u}}_i^k$. This part is unchanged. The fourth and final part consists of adjusting the ODT-resolved profiles so that the step-ending values of $V_i(y)$ and $v_i(y)$ are consistent with the new pressure-adjusted LES velocity field in the inner region.

Details of each of these four parts are given next.

4.6.1. Details of part 1

We begin by defining an ODT time step $\Delta t'$, and the associated ODT time-step index k'. The value of $\Delta t'$ is much smaller than the LES time step Δt so that a significant number of ODT time steps must be taken to advance in time from LES substep index $k-1$ to k, where $k=0$ represents the final state of the previous LES time step.

Each ODT time step consists of: (a) the evolution of the molecular equations from time t to $t+\Delta t'$, (b) the stochastic sampling procedure by which eddy events are determined, and (c) implementation of the selected eddy (if the sampling procedure determines that an eddy should be implemented).

The molecular equations are numerically integrated using the following explicit numerical approximation to Eq. (28):

$$\frac{v_i^{k'}-v_i^{k'-1}}{\Delta t'}=\frac{\delta}{\delta x_2}\left(\nu\frac{\delta v_i^{k'-1}}{\delta x_2}\right)-\frac{\delta}{\delta x_j}\left(V_j^{k'-1}v_i^{k'-1}\right)-\frac{PG_i}{\rho}, \tag{43}$$

where PG_i denotes the constant mean pressure gradient imposed on the flow, which in channel flow is zero for $i=2$ and 3. This term does not reflect the fluctuating pressure field that arises due to the turbulent fluctuations in the flow. This part of the pressure field is modeled through the pressure projection (see Sections 4.6.3 and 4.6.4). Second-order central differencing is used to compute all gradients, and boundary conditions are imposed as per Eqs. (31) and (32).

To compute the new ODT advecting velocity field $V_i^{k'}$, an alternative to Eq. (29) has been implemented that avoids the need to maintain a memory-intensive history of the instantaneous ODT velocity field.

Namely, a temporal 'mixing-cup' approach is adopted. Given the values of V_i at time index $k' - 1$, the values at k' are computed as

$$V_i^{k'} = \left(1 - \frac{\Delta t'}{\Delta t}\right) V_i^{k'-1} + \left(\frac{\Delta t'}{\Delta t}\right) v_i^{k'} \tag{44}$$

for $i = 1$ and 3 and Eq. (30) is applied for $i = 2$. We note that an alternative (not implemented here) to using Eq. (44) would be to hold $V_i^{k'}$ constant over the LES sub-step k to $k + 1$, and update these values at the same time the LES velocity field is updated.

After the molecular processes have evolved from time t to $t + \Delta t'$, the possibility of an eddy event is evaluated through the standard ODT stochastic-sampling procedure. However, allowable eddies are limited to those that extend into the inner region (as illustrated in Fig. 8), and the length of the largest possible eddy, $L_{\max}$, is a model parameter that, for now, must be specified. By design it must be of the order of the smallest length scale resolved by LES. Since this is a function of the numerics and filtering used in the LES code, its specific value must be likewise dependent.

If a trial-eddy location and length are chosen such that the eddy extends into the overlap region (see Fig. 8), ODT-resolved values are obtained in that region by linear interpolation of the LES field variables, as explained in Section 4.3.

Although eddy events implemented in the usual manner would modify property profiles in the LES/ODT overlap region, the modifications are not implemented in that region. Rather, statistics are gathered, as described next, that subsequently enable LES-scale implementation of the implied property transfers across LES control-volume interfaces. To compute the magnitude of the LES fluxes passed across the LES/ODT interface, ODT point values are currently used as if they are spatial averages over the ODT subvolumes illustrated in Fig. 7. As discussed in Section 4.3, this ensures important conservation requirements, but introduces a modeling artifact that may have impact on some details of the turbulence statistics.

As the ODT velocity fields are advanced in time from LES substep index $k - 1$ to k, momentum is transferred across the interface between the inner and overlap regions by three mechanisms: molecular diffusion, wall-normal advection, and eddy events. In addition, eddy events that extend to points greater than $y = 2\Delta Y$ induce momentum transfer across LES control-volume interfaces in the overlap region. In order for the ODT model to couple properly to the LES, a running sum of the net transport across all LES control-volume interfaces due to ODT processes must be maintained. For convenience in explaining the model, we define these sums as follows:

$S_i^n = i$th component momentum transport (per unit time, mass, and area) across an interface between a near-wall LES control volume n (where $n = 1$ denotes the inner region) and its adjacent $(n + 1)$-layer LES control volume.

$S_{\mathrm{D}_i}^n$ = that portion of S_i^n due entirely to the molecular-diffusive term of Eq. (43).

$S_{\mathrm{A}_i}^n$ = that portion of S_i^n due entirely to the advective term of Eq. (43).

$S_{\mathrm{E}_i}^n$ = that portion of S_i^n due entirely to ODT eddy events.

For $n = 1$, these sums are computed as

$$S_i^{1,k} = -\frac{\Delta t'}{\Delta t_k} \sum_{k'} \left(\nu \frac{\delta v_i^{k'-1}}{\delta x_2} \right)\Bigg|_{y=\Delta Y} + \frac{\Delta t'}{\Delta t_k} \sum_{k'} \left(V_2^{k'-1} v_i^{k'-1} \right)\Big|_{y=\Delta Y} + \frac{1}{\Delta t_k} \sum_m E_{m,i}^1 = S_{\mathrm{D}_i}^{1,k} + S_{\mathrm{A}_i}^{1,k} + S_{\mathrm{E}_i}^{1,k}, \tag{45}$$

where the additional superscript k has been added to denote that these quantities are computed during the interval Δt_k from LES substep $k - 1$ to k.

The only ODT process that can influence the LES equations at control volume interfaces greater than $y = \Delta Y$ is an eddy event. Thus for $n > 1$, $S_{\mathrm{D}_i}^n = S_{\mathrm{A}_i}^n = 0$, and we can write

$$S_i^{n,k} = S_{\mathrm{E}_i}^{n,k} = \frac{1}{\Delta t_k} \sum_m E_{m,i}^n \quad (\text{for } n > 1), \tag{46}$$

where Δt_k is the sub-time-step defined in Section 4.5 and $E_{m,i}^n$ denotes a transfer of i-component momentum across an interface between LES layers n and $n+1$ due to an eddy event m. It is easily computed as the x_2-integrated difference in momentum (after minus before) on one side of the interface following an eddy event.

At the end of part 1, the ODT velocity field has evolved due to advection, diffusion, and eddy events, but without a two-way coupling with the LES velocity field (which has been held constant). Part 1 is the ODT analog of solving Eq. (39) for the interim LES velocity $\hat{\bar{\boldsymbol{u}}}_i^k$ (part 2 below). Thus ODT values that have been evolved through the end of part one are in like manner hereafter denoted with a hat, e.g., $\hat{V}_i^k(y)$.

4.6.2. Details of part 2

In part 2 we solve for the interim LES velocity field $\hat{\bar{\boldsymbol{u}}}_i^k$ throughout the rest of the domain outside of the inner region, a process corresponding to the solution of Eq. (39), but with modifications associated with the LES/ODT overlap region that reflect ODT contributions to the LES surface fluxes in that region.

In the first LES layer of the overlap region, the transport across the LES/ODT interface at the top of the inner region is completely specified by the values computed in part 1. Also, the LES-specified advective flux across the top of this layer is enhanced by any contributions due to eddy events bridging this face. To account for these effects, Eq. (39) must be modified (in this layer only) as follows:

$$\begin{aligned}
\frac{\hat{\bar{\boldsymbol{u}}}_i^k - \bar{\boldsymbol{u}}_i^{k-1}}{\Delta t} = {} & \frac{(\nu + \nu_{\mathrm{S}})}{\Delta x_2} \left[\alpha_k \left(\frac{\delta \bar{\boldsymbol{u}}_i^{k-1}}{\delta x_2} \right) + \beta_k \left(\frac{\delta \hat{\bar{\boldsymbol{u}}}_i^k}{\delta x_2} \right) \right] \Bigg|_{x_2 = 2\Delta Y} - \frac{(\alpha_k + \beta_k)}{\Delta x_2} \left[S_{\mathrm{E}_i}^{2,k-1} - S_{\mathrm{E}_i}^{1,k-1} - S_{\mathrm{D}_i}^{1,k-1} \right] \\
& + (\alpha_k + \beta_k) \mathbf{L}_{xz}(\bar{\boldsymbol{u}}_i^{k-1}) - \gamma_k \mathbf{N}_{xz}(\bar{\boldsymbol{u}}_i^{k-1}) - \zeta_k \mathbf{N}_{xz}(\bar{\boldsymbol{u}}_i^{k-2}) \\
& - \frac{1}{\Delta x_2} \left[\gamma_k \left(\bar{\boldsymbol{u}}_i^{k-1} \bar{\boldsymbol{u}}_2^{k-1} \right) + \zeta_k \left(\bar{\boldsymbol{u}}_i^{k-2} \bar{\boldsymbol{u}}_2^{k-2} \right) \right] \Bigg|_{x_2 = 2\Delta Y} \\
& + \frac{(\alpha_k + \beta_k)}{\Delta x_2} \left[S_{\mathrm{A}_i}^{1,k-1} \right] - (\alpha_k + \beta_k) \frac{1}{\rho} \frac{\delta \bar{P}^{k-1}}{\delta x_i} - (\alpha_k + \beta_k) \frac{PG_i}{\rho}.
\end{aligned} \tag{47}$$

Here, the modified convection operator $\mathbf{N}_{xz}$ is defined as

$$\mathbf{N}_{xz}(\bar{\boldsymbol{u}}_i) = \frac{\delta}{\delta x_j} (\bar{\boldsymbol{u}}_i \bar{\boldsymbol{u}}_j), \tag{48}$$

where the right-hand side is summed over $j = 1$ and 3. Note that the difference between Eq. (39) and Eq. (47) is that all finite-difference terms associated with transport across the LES/ODT interface at the top of the inner region are replaced by the explicit sums computed in part 1, and the fluxes at the top of layer 2 are augmented by ODT contributions. For example, the first term on the RHS of line 1 of Eq. (47) are the diffusion terms (molecular and subgrid turbulent) across the $y = 2\Delta Y$ interface from the normal LES model. Because the wall-normal diffusion terms are integrated using a Crank-Nicholson scheme, there are both α_k and β_k contributions to the sub-time-step advancement. The last term on line 1 includes the eddy event contributions to the transport at $y = 2\Delta Y$ ($S_{\mathrm{E}_i}^{2,k-1}$) and $y = \Delta Y$ ($S_{\mathrm{E}_i}^{1,k-1}$), and the molecular diffusion term evaluated at the top of the ODT domain ($S_{\mathrm{D}_i}^{1,k-1}$). Similarly, wall-normal advection terms for $y = 2\Delta Y$ are found on line 3 (where both γ_k and ζ_k Runge–Kutta contributions are represented) and the ODT advective term for $y = \Delta Y$ ($S_{\mathrm{A}_i}^{1,k-1}$) is on line 4.

For all other LES volumes located within the overlap region (denoted by the superscript n, with $n > 2$), Eq. (39) is revised to look as follows:

$$\frac{\hat{\bar{u}}_i^k - \bar{u}_i^{k-1}}{\Delta t} = \alpha_k \mathbf{L}_y(\bar{u}_i^{k-1}) + \beta_k \mathbf{L}_y(\hat{\bar{u}}_i^k) - \frac{(\alpha_k+\beta_k)}{\Delta x_2}\left(S_{\mathrm{E}_i}^{n,k-1} - S_{\mathrm{E}_i}^{n-1,k-1}\right) + (\alpha_k+\beta_k)\mathbf{L}_{xz}(\bar{u}_i^{k-1}) - \gamma_k \mathbf{N}(\bar{u}_i^{k-1}) - \zeta_k \mathbf{N}(\bar{u}_i^{k-2}) - (\alpha_k+\beta_k)\frac{1}{\rho}\frac{\delta \bar{P}^{k-1}}{\delta x_i} - (\alpha_k+\beta_k)\frac{PG_i}{\rho}. \tag{49}$$

Note that the only difference between Eq. (39) and Eq. (49) is the addition of wall-normal transport terms coming from the ODT eddy events crossing LES boundaries as computed in part 1.

For LES volumes located outside of the LES/ODT overlap region, Eq. (39) is solved without modification.

4.6.3. Details of part 3

Part 3 requires values for the interim LES velocity field at all locations. To obtain these values in the ODT inner region, we apply Eq. (33) to the ODT advecting velocities, as follows:

$$\hat{\bar{u}}_i^k\Big|_{\text{inner region}} = \hat{\bar{V}}_i \equiv \frac{1}{N_{\mathrm{ODT}}}\sum_{m=1}^{N_{\mathrm{ODT}}} \hat{V}_{i,m} \tag{50}$$

for $i = 1$ and 3. Eq. (50) is not valid for the wall-normal velocity, $i = 2$, because of the definition of the ODT control volumes and locations as illustrated in Figs. 7 and 9. At the top of the inner region, the control surface through which the ODT advecting velocity $V_2|_{y=\Delta Y}$ fluxes fluid corresponds exactly to the LES interface through which the LES velocity component $\bar{u}_2$ fluxes fluid. The LES velocity is spatially filtered over a height ΔY, but the ODT advecting velocity corresponds to a cell of height $\Delta Y/N_{\mathrm{ODT}}$. For use in part 3, the ODT velocity is actually a more accurate approximation for the desired quantity because it is determined by enforcement of continuity, Eq. (30), reflecting ODT evolution since the previous LES time step. Thus we simply set

$$\hat{\bar{u}}_2^k\Big|_{\text{inner region}} = \hat{V}_2|_{y=\Delta Y}. \tag{51}$$

Part 3 begins by solving the discrete Poisson equation, Eq. (42), for ϕ^k. Knowing ϕ^k, Eq. (41) is integrated (with the rightmost term omitted, as explained in Section 4.5) to compute the change in pressure from $k-1$ to k. The new pressure is then given by

$$\bar{P}^k = \bar{P}^{k-1} + \frac{\rho\phi^k}{\alpha_k+\beta_k}. \tag{52}$$

Next, Eq. (40) can be applied to solve for the new velocity field:

$$\bar{u}_i^k = \hat{\bar{u}}_i^k - \Delta t\frac{\delta\phi^k}{\delta x_i}. \tag{53}$$

As indicated by Eqs. (50) and (51), $\hat{\bar{u}}_i^k$ in the inner region is determined solely by ODT quantities.

4.6.4. Details of part 4

The fourth and final part of the cycle consists of adjusting the ODT-resolved profiles of $\hat{V}_i^k(y)$ and $\hat{v}_i^k(y)$ to be consistent with the new pressure-adjusted velocity field in the inner region, but without significantly modifying the microstructure of the ODT profiles. Fig. 10 is useful in explaining how this is done.

Consider an ODT advective velocity field $\hat{V}_i^k(y)$ in the inner region after the completion of part 1. Since it has not yet been adjusted by the pressure-projection procedure, this profile is denoted with a hat. It has an average value $\hat{\bar{V}}_i^k$ (see Eq. (50)), but may have an irregular variation with y. A linear profile can be drawn

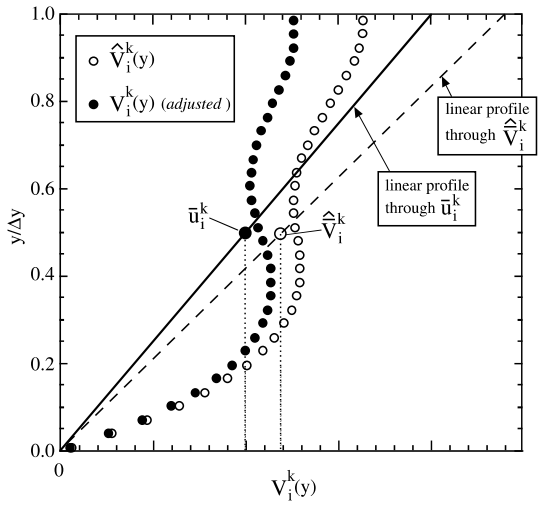

Fig. 10. Illustration of how an ODT velocity field is adjusted following a pressure-projection update.

from $y = 0$ to $y = \Delta Y$ that passes through the value $\hat{\bar{V}}_i^k$ at exactly $y = \Delta Y/2$. At any location y from the wall, one can compute a difference or 'variation' between the local value of $\hat{V}_i^k(y)$ and this linear function.

After part 3 is completed, a new adjusted value for $\bar{u}_i^k$ in the inner region is known. For $i = 1$ and 3, we impose the requirement that the difference (as a function of y) between the new $V_i^k(y)$ and the line $2\bar{u}_i^k y/\Delta Y$ is the same as the difference function $\hat{V}_i^k(y) - 2\hat{\bar{V}}_i^k y/\Delta Y$. Put another way, we obtain $V_i^k(y)$ by adding a linear profile to $\hat{V}_i^k(y)$ that enforces $\bar{V}_i^k = \bar{u}_i^k$, where the left-hand side of this equality represents the average of $V_i^k(y)$ over $0 \leqslant y \leqslant \Delta Y$, as defined by Eq. (33). This gives

$$V_i^k(y) - 2\frac{\bar{u}_i^k y}{\Delta Y} = \hat{V}_i^k(y) - 2\frac{\hat{\bar{V}}_i^k y}{\Delta Y} \tag{54}$$

for $i = 1$ and 3. After $V_1^k(y)$ and $V_3^k(y)$ are found, $V_2^k(y)$ is computed using Eq. (30).

To preserve the relationship between instantaneous and time-filtered ODT velocities when this adjustment is performed, the ODT instantaneous velocity profiles are adjusted based on the relationship

$$v_i^k(y) - 2\frac{\bar{u}_i^k y}{\Delta Y} = \hat{v}_i^k(y) - 2\frac{\hat{\bar{V}}_i^k y}{\Delta Y} \tag{55}$$

for $i = 1$ and 3. $v_2^k(y)$ is not adjusted because it is not kinematically linked, through relations like Eqs. (44) and (50), to LES-scale processes.

At the end of part 4, all values have been advanced from LES sub-time-step $k - 1$ to k.

4.7. Remarks

The LES/ODT subprocesses and couplings are formulated to be complementary, each providing the other with the information needed to simulate flow evolution within the range of scales that it represents. However, we note here that neither the ODT momentum equation, Eq. (28), nor the adjustment in part 4 communicates the large-scale forcing to the wall-normal ($i = 2$) ODT velocity component. It is neither necessary nor desirable to couple v_2 to these forcings. Continuity is sufficient to determine the advective velocity V_2 that provides an LES-scale representation of the effect of ODT evolution on wall-normal flow.

As in ODT stand-alone implementation, v_2 is a kinetic-energy reservoir that is incorporated to improve the fidelity of the ODT representation of energy transfers among the three velocity components. Owing to the distinctive role of v_2 in the formulation of the ODT event-rate distribution, v_2 may have additional physical significance in future applications to transition and other phenomena that are sensitive to details of this formulation.

5. Coupled LES/ODT simulations of channel flow

Fully developed turbulent channel flow has been studied extensively in the past and both experimental data [12,45] and numerical DNS data [33] are available for comparison purposes. Stand-alone ODT results for this flow are presented in Section 2.4. Here we present results based on the coupled LES/ODT model.

The LES computational domain is 2π, $2\pi/3$, and 2 in the streamwise (x), spanwise (z), and wall-normal (y) directions, respectively. Calculations were performed at Reynolds numbers based on friction velocity ranging from 395 to 10,000 in order to test the modeling over a wide range of Reynolds numbers. For all but the highest-Reynolds-number flows considered, the domain is discretized by a relatively coarse $32 \times 32 \times 32$ uniform grid in the streamwise, spanwise, and wall-normal directions. As the Reynolds number is increased, a smaller portion of the total kinetic energy is captured on the LES grid. Thus for the higher Reynolds-number flows the resolution was increased and a uniform $48 \times 48 \times 64$ discretization was used. Although more refined LES meshes could have been chosen, an important purpose of this work is to test the new approach under coarsely meshed LES conditions representative of typical mesh resolutions expected in real-life applications. This is the same rationale invoked by other wall-model researchers (e.g., [8,9]) whose domain size and mesh resolutions have been similar. This choice is also supported by the study of wall modeling using suboptimal control theory by Nicoud et al. [34] who showed that a $32 \times 32 \times 32$ uniform grid was adequate to yield reasonable mean flow predictions in channel flow at friction-velocity based Reynolds numbers ranging from 640 to 20,000.

To resolve the ODT domain properly, an ODT near-wall mesh spacing of approximately 1 wall unit (y^+) was found to be sufficient to achieve grid-independent results.

To perform a set of coupled LES/ODT calculations, the ODT model constants C, Z, α, and $L_{\max}$ must be specified. $\alpha = 2/3$ is used for all results shown in this section, and Z is again assigned the value 98. These values, together with the choice $C = 12.73$, yield a good fit of DNS data by stand-alone ODT (Section 2.4). For LES/ODT, it is found that a slightly lower value of the overall rate constant, $C = 9.9$, is the best value for matching the DNS mean velocity profile at $Re_\tau = 590$. This adjustment reflects the impact of the large scale LES forcings on the ODT model when coupled together. Although the adjustment is relatively small, it nevertheless is sufficient to imply a distinction between the coupling of near-wall and bulk regions in stand-alone ODT and LES/ODT, respectively.

The coupled LES/ODT model requires a different approach for determining the maximum eddy length parameter, $L_{\max}$, than was used when doing stand-alone ODT calculations. This is because the integral length scale of the flow (e.g, the channel width) is no longer an appropriate measure of this parameter. Instead, $L_{\max}$ is now associated with the LES filter width, and determines the length of the overlap region (as illustrated in Fig. 1(c)). It corresponds physically to the largest length scale captured by ODT, and should also correspond approximately to the smallest length scales resolved by the LES.

To determine the appropriate value of $L_{\max}$, a simple parametric sensitivity study was performed. Fig. 11 illustrates the results of this exercise for flow at $Re_\tau = 590$. Four different simulations were performed, keeping all other values and conditions constant except for the value of $L_{\max}$. A large change is seen as $L_{\max}$ is increased from $2\Delta Y$ to $3\Delta Y$, but very little difference is seen as its value is increased from $3.5\Delta Y$ to $4\Delta Y$. These results are consistent with the notion that this value should correspond approximately to the smallest

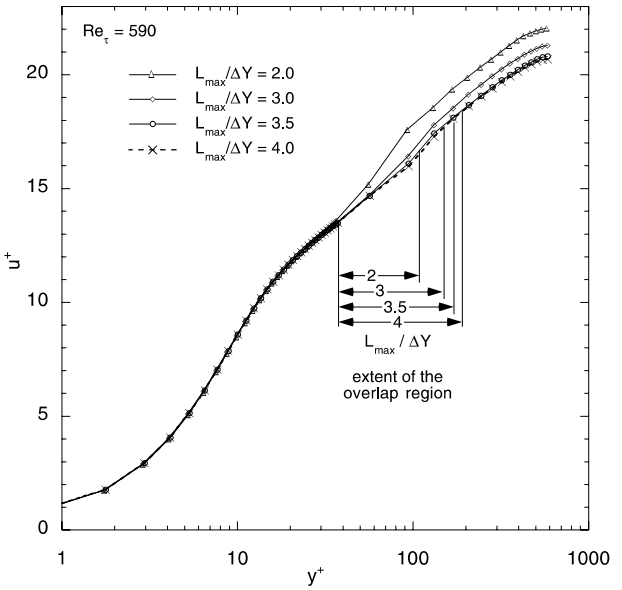

Fig. 11. Sensitivity of the LES/ODT mean velocity profiles to different values of $L_{\max}$.

length scales resolved by the LES on the numerical mesh. For all other calculations shown here we use the value $L_{\max} = 3.5\Delta Y$.

Table 1 summarizes six calculations performed as a test of the current LES/ODT coupled model. In each of these runs, the values of C, Z, α, and $L_{\max}$ were held fixed at the values specified above. In each case, the simulation was started by specifying a randomly perturbed initial velocity profile and then allowing the computation to proceed without taking statistics until the initial transient behavior had settled out and the time-averaged wall stress balanced the mean pressure gradient exactly. This typically occurred within several hundred non-dimensional time units (based on bulk velocity and channel half width). Statistics were then taken over non-dimensional time periods of about 300 time units. As a final check, the calculations were then continued over a similar time period and the results compared so as to assure that the statistics were adequately converged.

For each calculation both an LES time step Δt and a smaller ODT time step $\Delta t'$ must be appropriately chosen. Here, the LES time step was specified such that the maximum CFL condition was approximately 0.5. Because the meshes used are relatively coarse, the LES time step is comparatively large, and adequate statistical samples (see above) are obtained for runs of only a few thousand LES time steps. The smaller ODT time step $\Delta t'$ was set based on the need to keep the mean acceptance probability $\bar{P}_a$ small (see Section

Table 1
Computed cases

Case	Re_τ	Re	N_{ODT}	$\Delta y^+_{\mathrm{ODT}}$	N_x	N_y	N_z
A	395	14,020	24	1.03	32	32	32
B	590	22,472	32	1.15	32	32	32
C	1200	49,336	64	1.17	32	32	32
D	2400	108,624	128	1.17	32	32	32
E	4800	234,332	128	1.17	48	64	48
F	10,000	534,224	256	1.17	48	64	48

2.3), and for convenience in maintaining consistency with the Runge–Kutta time-advancement coefficients (Section 4.5). Specifically, $\Delta t'$ was chosen for these calculations so that: (1) $\bar{P}_a \leqslant 0.05$ and (2) $\Delta t/\Delta t'$ was divisible by 15. Numerical stability requirements for the discrete ODT equations (Eq. (43)) were also monitored during each run to assure that the time step based on these conditions was sufficiently small to avoid stability problems.

All calculations were performed on single-processor SGI workstations with run times varying from several hours for the lower-Reynolds-number flows to several days for the highest-Reynolds-number flows. (Note that because extensive optimization of the code and model algorithms has not yet been attempted, some improvement in run times is expected when this is done.) The comparative computational cost of the ODT near-wall model relative to the bulk-flow LES model depends upon three things: (1) the surface-to-volume ratio of the particular flow being modeled, (2) the size of the LES mesh (which also determines the spatial domain near the wall that ODT must simulate), and (3) the flow Reynolds number (which determines the length and time scales that must be resolved at the wall). Complicating the assessment of these relative costs is the fact that the inner region ODT costs scale with problem size in a distinctly different way than the bulk-flow LES calculation does.

Because cases A–D were calculated on the same uniform LES mesh the bulk-flow LES portion of the CPU cost per time step remained constant. For our reference SGI workstation this cost was 0.53 s. Likewise, cases E and F shared the same bulk-flow LES CPU cost per time step (4.83 s). However, because the flow Reynolds numbers were different for each run, the near-wall ODT mesh size, time steps, and CPU costs varied with each run. Initially, it was expected that for a given flow configuration (e.g., channel flow) and associated fixed LES mesh, that the near-wall ODT model costs would scale as Re_τ^2 – reflecting the linear increase in ODT nodes in 1 spatial dimension and also a linear decrease in ODT time step. However, the actual increase in CPU cost scaled approximately as $Re_\tau^{2.3}$. This variation from expected behavior was due to a somewhat larger than expected rate-of-decrease in ODT time-step size required to maintain the desired acceptance probability P_a as higher Reynolds number flows were calculated. For comparison, the ODT portion of the CPU cost per LES time step was 0.36 s for case B and 41.4 s for case E.

To illustrate the results of the overall LES/ODT modeling approach for channel flow, the figures that follow generally present data over the entire channel flow domain (i.e., wall to centerline). However, our focus is primarily on the ODT-based near-wall model and its transition to the bulk-flow LES. We note that the performance of the LES model in the outer-flow region away from the wall is not a new contribution, but is simply consistent with what would be expected from the dynamic SGS model (and the second-order numerical methods used) for the conditions and relatively coarse meshes specified.

Fig. 12 helps illuminate the dynamics of the coupled LES/ODT model by showing near-wall mean and instantaneous velocity profiles for an illustrative calculation at $Re_\tau = 1200$. In contrast to the smoothly varying time-averaged profile that is shown, instantaneous profiles are highly irregular. Of particular note are the wrinkling effects of eddy events on the velocity profiles in the ODT inner region. At the particular instant shown, the effects of both large and small eddy events can be clearly seen. Furthermore, the smoothing effect of molecular processes over time can be seen and contrasted to the sharp gradients imposed by recent eddy events.

Fig. 13 presents LES/ODT model results for the mean velocity profiles over the Reynolds-number range indicated in Table 1. For cases A and B, the DNS data of Moser et al. [33] are available and are used for direct comparison. For all cases, the inner law, $u^+ = y^+$, and a commonly accepted [12] log law, $u^+ = 2.44\ln(y^+) + 5.2$, are also plotted for comparison. Data symbols are used to denote LES/ODT node-point values in order to highlight the increased resolution of the model in the ODT domain.

When compared with results for the mean velocity profiles obtained from alternative LES near-wall models, the results demonstrated in Fig. 13 are excellent. For example, in evaluating several near-wall models (including the two-layer model of [5]) which were coupled to the same standard dynamic SGS model used here, Cabot and Moin [9] noted that results are generally poor for the mean streamwise velocity in the

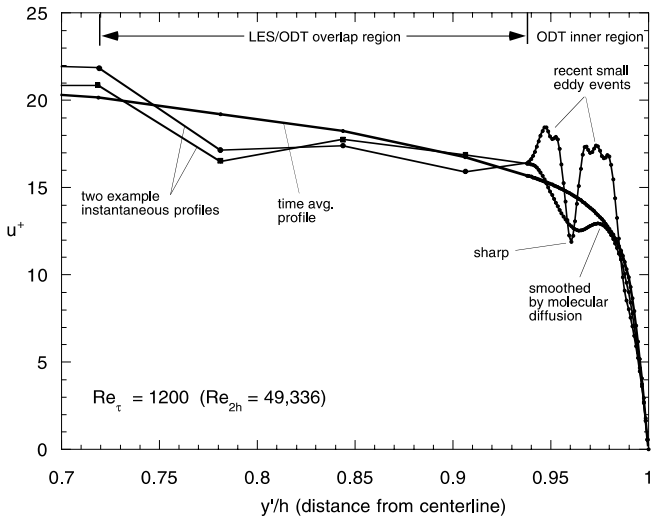

Fig. 12. Near-wall mean and sample instantaneous velocity profiles.

first few off-wall grid points. The main point of concern was that the near-wall slope was too shallow, leading to a low intercept in the logarithmic region. (Note that improvements were made by adjusting the near-wall dynamic coefficient [9].) This can be compared with the LES/ODT results shown here where near-wall mean velocities are predicted quite well with no adjustments to the near-wall LES model coefficients. At all Reynolds numbers, the simulations produce a physically realistic viscous sublayer smoothly transitioning through the buffer zone into a log layer. No discontinuity in slope is seen between the highly resolved ODT inner region and the first and second near-wall LES nodes, which lie in the LES/ODT overlap region. However, between the second and third LES nodal values (near the edge of the LES/ODT overlap region), a slight rise in the mean profile can be noticed. This occurs as the modeling of turbulent transport shifts from being primarily captured by 1D ODT eddy events to the 3D LES flow model, and merits further study to be better understood. Although detectable, this artifact is small when compared to the large buffer layer that appears in the detached-eddy simulation (DES) mean-velocity results for channel flow presented by Nikitin et al. [35] and is further discussed in [37]. In DES, as the flow transitions from the inner-region RANS model to the outer-region LES model, a major change in the mean velocity gradient is seen, leading to two distinct logarithmic layers, the second of which is artificially high.

Fig. 14 is a plot of the friction coefficient as a function of Reynolds number. The LES/ODT results, extending over a wide range of the bulk-flow Reynolds number, are in good agreement with DNS and experimental results. At the highest Reynolds numbers (cases E and F), the LES/ODT results suggest a trend that is slightly high compared to the correlation of Dean [12]. This difference is most likely due to the poor LES resolution of the wake region, leading to a comparatively lower bulk velocity and thus a higher friction coefficient (see [8] for a discussion of this topic).

Figs. 15–19 are plots of root-mean-square (RMS) velocity fluctuation profiles, normalized by u_τ. These results are important because they help characterize the near-wall dynamic behavior that cannot be obtained from low-order RANS-based models. The dynamic fluctuations that are reflected in these profiles are also important to multiphysics applications in which physical processes such as heat transfer and chemical reactions are sensitive to these fluctuations.

In Fig. 15 LES/ODT-computed RMS velocity fluctuation profiles at $Re_\tau = 590$ are compared with the DNS calculations of Moser et al. [33] and results of the previously discussed stand-alone ODT calculations

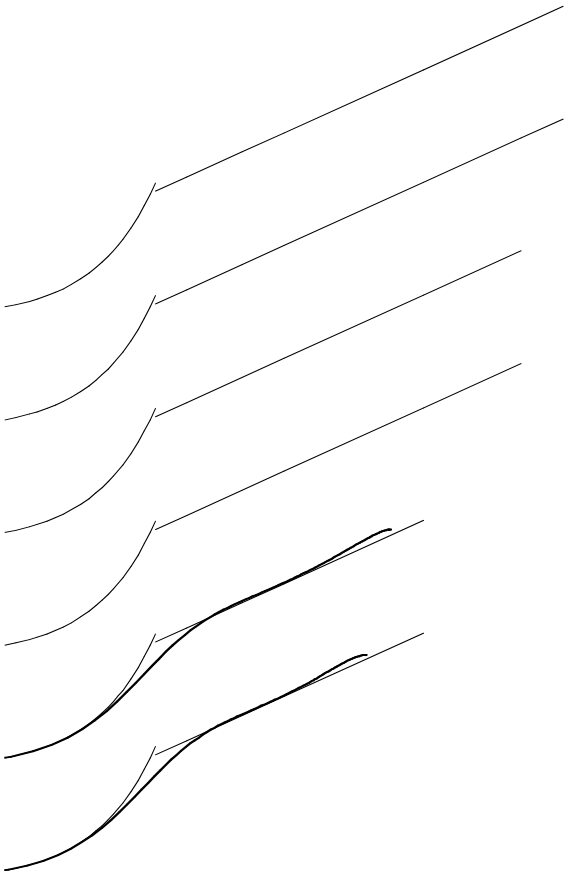

(Section 2.4). We begin by noting that overall, the magnitudes and shapes of the LES/ODT RMS velocity fluctuation profiles compare quite favorably with DNS and show noticeable improvement over stand-alone ODT results. This improvement reflects the impact of large-scale LES forcings on the ODT model when coupled together, and highlights the complementary nature of the combined modeling approach.

In comparing LES/ODT results for u_{rms} with DNS, we can see (1) perfect agreement for $y^+ < 9$, (2) a somewhat flattened peak region where the LES/ODT results are about 10 percent lower than DNS, (3) good agreement (although slightly high) in the central channel region ($y^+ > 200$), and (4) a rise of LES/ODT values compared to DNS as the wall is approached from the central region, but a return to the DNS profile in the LES/ODT overlap region. Elevated values of u_{rms} near the wall are symptomatic of under-resolved LES (e.g., [29]); this figure illustrates clearly how the ODT subgrid model coupling acts to suppress this problem.

For stand-alone ODT, only a single profile is plotted for both wall-normal v_{rms} and spanwise w_{rms} velocity fluctuations because in the current three-component model, the statistics for these two components

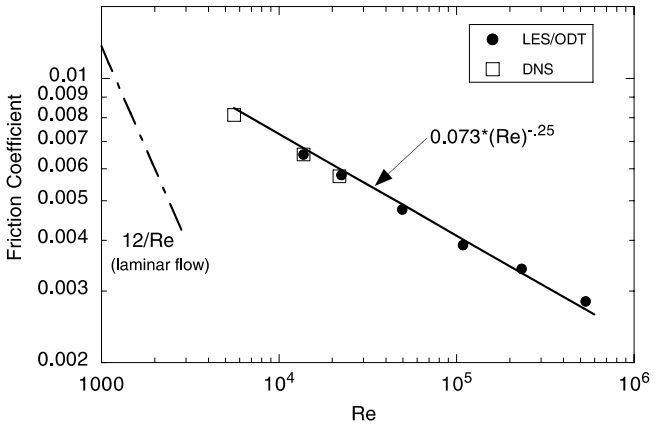

Fig. 14. LES/ODT computed friction coefficient for channel flow compared to DNS data [33] and the correlation of Dean [12]. Here, Re is based on the bulk velocity and the channel width ($2h$).

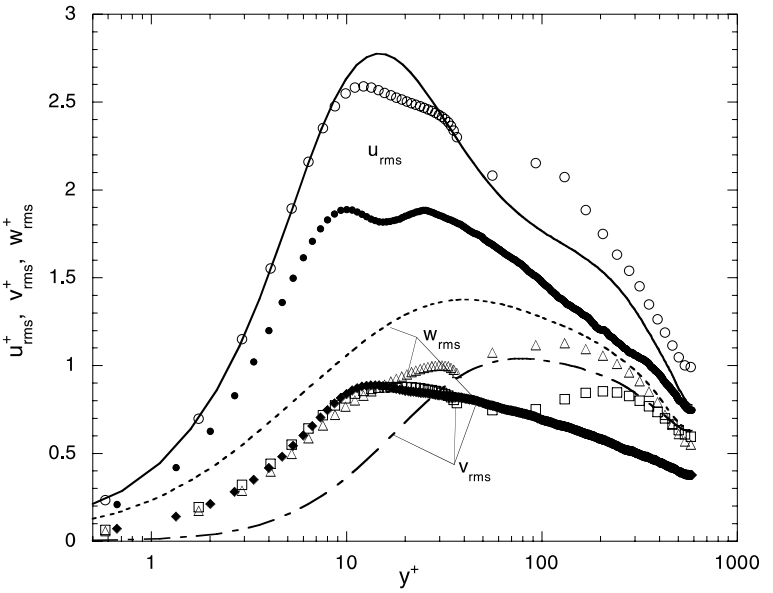

Fig. 15. Root-mean-square velocity fluctuation profiles normalized by the friction velocity for $Re_\tau = 590$ and computed from LES/ODT (open symbols), ODT stand-alone (filled symbols), and DNS [33] (solid and dashed lines).

are identical. Their near-wall behavior is intermediate between the DNS data for v_{rms} and w_{rms}. However, for LES/ODT the profiles are not identical because they couple to distinctly different LES velocity fields. This can be seen in Fig. 15 where very near the wall, the profiles are almost identical, but as the top of the inner region is approached and the coupling to LES becomes stronger, the profiles diverge. We also note a small dip in the w_{rms} profile at the upper edge of the inner region, and a subsequent discontinuity in the slope (also seen in each of the other profiles). This reflects the abrupt jump from a finely resolved ODT mesh to the much coarser LES mesh and may be associated with the rather simple interfacial boundary conditions applied.

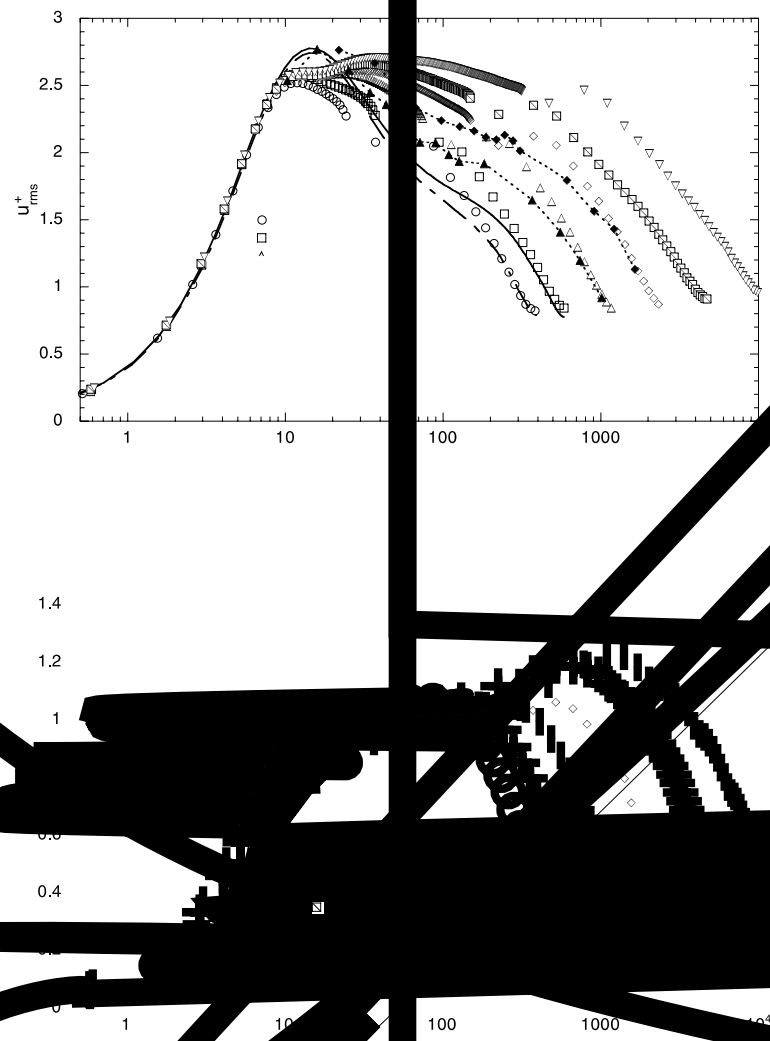

Fig. 17. Spanwise root-mean-square velocity fluctuation profiles normalized by the friction velocity.

Fig. 16, ... results for w_{rms} from simulations at six Reynolds numbers are compared to the DNS of Moser et al. [23] and the data of Wei and Willmarth [...]. (Unfortunately, reliable near-wall data for DNS velocity fluctuations are not currently available for channel flow at high Reynolds numbers comparable to Cases E and F.) This figure illustrates that most of the characteristic peaks present in computing on Fig. 15 remain apparent for all cases considered. All cases collapse to a single curve for $y^+ < 9$, and show a somewhat [...] region relative to DNS and measurements. [...] clear transition from scaling on inner variables near the wall to the qualitatively correct Reynolds number dependence away from the wall. Although not plotted here, away from the wall the data collapse to a single curve if plotted in global coordinates (y) [28] and show good agreement with the DNS and experimental data.

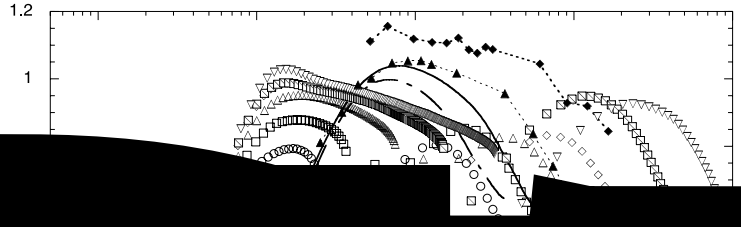

Wall-norm
vecting velo

nce again
ained by
sistently
alues of
rofiles
r-wall

the
lata
a

v_{rms} component be-

tween the DNS v_{rms} and w_{rms}. At the top of the inner region, the profiles tend to dip due to the increasing influence of the LES. In the overlap region the profiles gradually converge to the LES dominated behavior, which is broadly consistent with the available data in the central portion of the channel.

In constructing the LES/ODT subgrid model, a set of advecting velocities is defined in Section 4.2. V_1 and V_3 are based directly on v_1 and v_3 respectively (see Eq. (29)), and results show that the RMS velocity fluctuation profiles based on V_1 and V_3 are virtually the same as the RMS profiles based on v_1 and v_3. However, the advecting wall-normal velocity component V_2 is based on satisfying continuity in the ODT sub-control volumes (see Eq. (30)), and is not directly tied to the ODT component v_2. Fig. 19 is identical to Fig. 18 except that V_{rms} is plotted in the inner region instead of v_{rms}. As can be seen, these profiles are quite different. Here we see that the LES/ODT values for V_{rms} are consistently lower than the DNS data. In fact, the DNS data falls intermediate between the values for V_{rms} shown here and the values for v_{rms} shown in Fig. 18. Also of note is the strong Reynolds-number dependence of V_{rms} even in the very near-wall region. This points out that V_2 is subject to large-scale influences even near the wall, which may be an artifact of the LES-scale averaging (V_2 is an average over an X–Z face, as illustrated in Fig. 7) or the simple profile assumptions made in constructing the velocity adjustment described in Section 4.6.4. In this context, V_2 may be viewed as an auxiliary quantity used to enforce continuity. v_2 provides a better, though approximate, representation of wall-normal single-point flow statistics.

6. Discussion

In this paper we have presented a novel approach to LES wall modeling based on the ODT model of Kerstein et al. [27], and described details and results from our first implementation of a practical model based on these ideas. In this regard, a variety of physical modeling and numerical implementation issues have been addressed. As with all models, the ODT-based model presented here invokes approximations of the near-wall flow physics which lead to some differences when compared to detailed DNS or experimental data. However, an important distinguishing attribute of this approach is that Reynolds averaging and all associated modeling approximations (such as an eddy-viscosity model) are avoided. Therefore, detailed comparisons can be made with experimental and DNS turbulence data in the very-near-wall region that are not possible with previous approaches. Furthermore, because near-wall velocity and scaler fluctuations are intrinsic elements of the model, the approach holds promise as a method for treating certain multiphysics problems that would be difficult to simulate well with other wall models.

As an initial test of the model, computed results for turbulent channel flow have been compared to DNS and experimental data over a large range of Reynolds numbers. Although this problem is geometrically simple, it is important because detailed data (including higher-moment turbulence data) is available, and it is a standard problem against which almost all other LES wall-models have also been tested. With respect to the mean velocity and friction coefficient, the results obtained demonstrate the excellent performance of the present model when compared with previous models and correlations. Furthermore, near-wall results for higher-order statistics are shown to be directly comparable to DNS data, and clearly illustrate that the near-wall ODT model dynamics are intimately coupled with the dynamics of the outer-flow LES, allowing for two-way interactions that produce near-wall turbulence statistics and scalings that are notably improved over ODT as a stand-alone model. However, despite these encouraging results, additional tests and comparisons against data for more challenging flow configurations involving separation, reattachment, and other related effects are needed before the relative performance and cost of this new model can be thoroughly understood. It is expected that more complicated flows will be well represented because LES/ODT incorporates a basic attribute that is essential for a robust near-wall treatment, namely, physically rea-

sonable time-lagged response to transient bulk forcings. For example, if the bulk flow undergoes a reversal, this transient will be communicated gradually inward toward the wall by ODT processes. Reversal of the wall-shear direction will occur after a period of nonmonotonic near-wall flow structure (superimposed on the ever-present nonmonotonicity due to turbulent fluctuations).

The computational cost of the present model relative to the bulk-flow LES model depends upon three things: (1) the surface-to-volume ratio of the particular flow being modeled, (2) the size of the LES mesh (which also determines the spatial domain near the wall that ODT must simulate), and (3) the flow Reynolds number (which determines the length and time scales that must be resolved at the wall). Although direct comparisons with other wall models are not performed here, the computational cost of the present model clearly lies intermediate between DES and wall-stress models (including the two-layer model), and fully resolved LES of the near-wall region. The major additional cost over models such as DES and the two-layer model is associated with temporally resolving the eddy event frequencies down to the smallest scales.

With regard to computational cost, it is useful to make several additional comments. First, because the LES mesh does not require near-wall refinement, the effective LES time step associated with the CFL condition can be much larger. This is a benefit shared by all wall models and, by itself, introduces a significant cost savings over an LES in which the near-wall region is fully resolved. Second, the cost of doing the LES portion of the problem scales with problem size (i.e., the mesh) differently than the ODT part. This scaling will depend strongly on the numerical (and potentially parallel) algorithms used in the LES code, but is not expected to scale as favorably as does the ODT part of the problem (which for the present model scales approximately as $Re_\tau^{2.3}$). For a given geometry at a fixed Reynolds number the overall cost becomes a tradeoff – increasing the resolution of the LES mesh will increase the cost of the LES portion, but decrease the relative cost of the wall model because the number of ODT points required in the wall-normal direction is reduced. Because these scale differently and because the relative importance of the bulk flow compared to the near-wall region depends upon the purpose of the simulation, a general rule is difficult to specify. To illustrate this tradeoff we compare the costs of case D ($Re_\tau = 2400$, $32 \times 32 \times 32$ LES grid, 128 ODT points per ODT line) with a new case D′, where the LES mesh is increased to $64 \times 64 \times 64$ but which now only has 64 ODT points per ODT line. For the original case D the near-wall model was about 95% of an overall simulation cost of approximately 15 s per reference time unit – a relative cost that was the highest of all the cases performed. For case D′, simple tests on our reference workstation show that the near-wall model (now associated with four times as many ODT lines but with half as many ODT points per line) is only approximately 35% of the new overall simulation cost of about 70 s per reference time unit. (Note that for a constant CFL, twice as many LES time steps per reference time unit are required for case D′.) This illustrates that, in general, the bigger the overall LES problem, the smaller the relative cost of doing the near-wall portion. Our experience here with channel flow suggests that the cost of an ODT-based wall model for large LES problems will be roughly the same cost as the LES bulk-flow portion of the calculation. (See [28] for additional details on this topic.)

Future efforts will focus on questions in several areas. First, additional tests in more complex flow configurations are needed (as described above). Second, model improvements such as non-uniform ODT mesh spacing (to reduce ODT costs) and refined methods for coupling to the LES in the overlap region are being explored. Third, as improvements to ODT are developed (such as an improved representation of the differences between v_{rms} and w_{rms}), they will be incorporated and would be expected to favorably affect the coupled LES/ODT model described here. Finally, there are certain methodological issues yet to be addressed, such as the existence of grid-independent solutions as grid resolution and time-step refinement are increased. LES formulations applicable to flows of interest have some inherent difficulties in this regard. It is important to understand whether the ODT near-wall closure worsens or lessens these difficulties.

Stand-alone ODT is particularly useful for simulating turbulence-microscale interactions due to its fully resolved treatment of fine-scale phenomena. In particular, molecular mixing occurs solely by means of

physically realistic diffusive transport because advective processes are represented by a purely advective model construct (eddy events) rather than by eddy diffusivity. Accordingly, stand-alone ODT is especially advantageous for turbulent combustion modeling [15]. However, the near-wall formulation introduced here, though suitable for momentum closure, may not be similarly advantageous for subgrid combustion closure. The lateral advection that couples ODT sub-volumes in adjacent LES control volumes (Section 4.2) is implemented at LES spatial resolution and therefore introduces numerical diffusion far in excess of ODT-resolved viscous transport. This numerical diffusion does not necessarily dominate ODT-resolved eddy transport in the vertical direction (though this issue merits further investigation), but it certainly dominates mixing by molecular diffusion. A robust closure for mixing-sensitive processes such as combustion must avoid this artifact. An approach that satisfies this requirement has been formulated [26] and will be implemented and tested in the future.

Acknowledgements

The authors would like to thank J. Baggett and W. Cabot for providing the LES code used in this work and for providing other assistance during their affiliation with the Center for Turbulence Research at Stanford University. This work was supported by the Department of Energy Laboratory Directed Research and Development (LDRD) program at Sandia National Laboratories and by the Division of Chemical Sciences, Geosciences, and Biosciences, Office of Basic Energy Sciences, US Department of Energy.

References

[1] W.T. Ashurst, A.R. Kerstein, One-dimensional turbulence: variable-density formulation and application to mixing layers, J. Fluid Mech., 2002, submitted for publication.
[2] J.S. Baggett, On the feasibility of merging LES with RANS for the near-wall region of attached turbulent flows, Annual Research Briefs 1998, Center for Turbulence Research, Stanford University, Palo Alto, California, 1998, p. 267.
[3] J.S. Baggett, J. Jimenez, A.G. Kravchenko, Resolution requirements for large-eddy simulations of shear flows. Annual Research Briefs 1997, Center for Turbulence Research, Stanford University, Palo Alto, California, 1997, p. 51.
[4] E. Balaras, C. Benocci, Subgrid-scale models in finite-difference simulations of complex wall bounded flows, AGARD CP 551 Neuilly-Sur-Seine, France:AGARD, 1994, pp. 2.1–2.5.
[5] E. Balaras, C. Benocci, U. Piomelli, Two-layer approximate boundary conditions for large eddy simulations, AIAA J. 34 (1996) 1111.
[6] W. Cabot, Large-eddy simulations with wall models. Annual Research Briefs 1995, Center for Turbulence Research, Stanford University, Palo Alto, California, 1995, p. 41.
[7] W. Cabot, Near-wall models in large-eddy simulations of flow behind a backward-facing step. Annual Research Briefs 1996, Center for Turbulence Research, Stanford University, Palo Alto, California, 1996, p. 199.
[8] W. Cabot, J. Jimenez, and J.S. Baggett. On wakes and near-wall behavior in coarse large-eddy simulation of channel flow with wall models and second-order finite-difference methods, Annual Research Briefs 1999, Center for Turbulence Research, Stanford University, Palo Alto, California, 1999, p. 343.
[9] W. Cabot, P. Moin, Approximate wall boundary conditions in the large-eddy simulation of high Reynolds number flow, Flow Turb. Combust. 63 (1999) 269.
[10] D.R. Chapman, Computational aerodynamics development and outlook, AIAA J. 17 (1979) 1293.
[11] M. Ciofalo, Large-eddy simulation: A critical survey of models and applications, Adv. Heat Transf. 25 (1994) 321.
[12] R.B. Dean, Reynolds number dependence of skin friction and other bulk flow variables in two-dimensional rectangular duct flow, J. Fluids Eng. Trans. ASME 100 (1978) 215.
[13] J.W. Deardorff, A numerical study of three-dimensional turbulent channel flow at large Reynolds numbers, J. Fluid Mech. 41 (1970) 453.
[14] J.K. Dukowicz, A.S. Dvinsky, Approximate factorization as a high-order splitting for the implicit incompressible flow equations, J. Comput. Phys. 102 (1992) 336.
[15] T. Echekki, A.R. Kerstein, J.-Y. Chen, T.D. Dreeben, One-dimensional turbulence simulation of turbulent jet diffusion flames: model formulation and illustrative applications, Comb. Flame 125 (2001) 1083.

[16] M. Germano, U. Piomelli, P. Moin, W.H. Cabot, A dynamic subgrid-scale eddy viscosity model, Phys. Fluids A 3 (1991) 1760.
[17] S. Ghosal, T.S. Lund, P. Moin, K. Akselvoll, A dynamic localization model for large-eddy simulation of turbulent flows, J. Fluid Mech. 286 (1995) 229.
[18] S. Ghosal, P. Moin, The basic equations for the large eddy simulation of turbulent flows in complex geometries, J. Comp. Phys. 118 (1995) 24.
[19] G. Grotzbach, Direct numerical and large eddy simulation of turbulent channel flows, in: N.P. Chereminisoff (Ed.), Encyclopedia of Fluid Mechanics, Gulf Publ., West Orange, NJ, 1987, p. 1337.
[20] F.H. Harlow, J.E. Welch, Numerical calculation of time-dependent viscous incompressible flow of fluid with free surface, Phys. Fluids 8 (1965) 2182.
[21] G. Hoffmann, C. Benocci, Approximate wall boundary conditions for large eddy simulations, in: R. Benzi (Ed.), Advances in Turbulence V, Kluwer Academic Publishers, Dordrecht, 1995, p. 222.
[22] J. Jimenez, R. Moser, LES: where are we and what can we expect? AIAA paper 98-2891, 1998.
[23] J. Van Kan, A second order accurate pressure-correction scheme for viscous incompressible flow, SIAM J. Sci. Stat. Comp. 7 (1986) 870.
[24] A.R. Kerstein, Linear-eddy modeling of turbulent transport. Part 6. Microstructure of diffusive scaler mixing flields, J. Fluid Mech. 231 (1991) 361.
[25] A.R. Kerstein, One-dimensional turbulence: model formulation and application to homogeneous turbulence, shear flows, and buoyant stratified flows, J. Fluid Mech. 392 (1999) 277.
[26] A.R. Kerstein, One-dimensional turbulence: a new approach to high-fidelity subgrid closure of turbulent flow simulations, Comput. Phys. Commun. 148 (2002) 1.
[27] A.R. Kerstein, W.T. Ashurst, S. Wunsch, V. Nilsen, One-dimensional turbulence: vector formulation and application to free shear flows, J. Fluid Mech. 447 (2001) 85.
[28] A.R. Kerstein, R.C. Schmidt, S. Wunsch, W.T. Ashurst, V. Nilsen, T.D. Dreeben, High-resolution modeling of multiscale transient phenomena in turbulent boundary layers. Report No. SAND2001-8108, Sandia National Laboratories, 2001.
[29] A.G. Kravchenko, P. Moin, R. Moser, Zonal embedded grids for numerical simulations of wall-bounded turbulent flows, J. Comput. Phys. 127 (1996) 412.
[30] D.K. Lilly, A proposed modification of the Germano subgrid-scale closure method, Phys. Fluids A 4 (1992) 633.
[31] P.J. Mason, N.S. Callen, On the magnitude of the subgrid-scale eddy coefficient in large-eddy simulations of channel flow, J. Fluid Mech. 162 (1986) 439.
[32] Y. Morinishi, Conservative properties of finite difference schemes for incompressible flow, Annual Research Briefs 1995, Center for Turbulence Research, Stanford University, Palo Alto, California, 1995, p. 121.
[33] R.D. Moser, J. Kim, N.N. Mansour, Direct numerical simulation of turbulent channel flow up to $Re = 590$, Phys. Fluids 11 (1999) 943.
[34] F. Nicoud, J.S. Baggett, P. Moin, W. Cabot, Large eddy simulation wall-modeling based on suboptimal control theory and linear stochastic estimation, Phys. Fluids 13 (2001) 2968.
[35] N. Nikitin, F. Nicoud, B. Wasistho, K. Squires, P. Spalart, An approach to wall modeling in large-eddy simulations, Phys. Fluids 12 (2000) 1629.
[36] S.V. Patankar, Numerical Heat Transfer and Fluid Flow, Hemisphere, Washington, DC, 1981.
[37] U. Piomelli, E. Balaras, Wall-layer models for large-eddy simulations, Ann. Rev. Fluid Mech. 34 (2002) 349.
[38] U. Piomelli, J. Ferziger, P. Moin, J. Kim, New approximate boundary conditions for large eddy simulations of wall-bounded flows, Phys. Fluids A 1 (1989) 1061.
[39] P. Quemere, P. Sagaut, V. Couailler, A new multi-domain/multi-resolution method for large-eddy simulation, Int. J. Numer. Meth. Fluids 36 (2001) 391.
[40] S.M. Ross, A Course in Simulation, Macmillan, New York, 1990.
[41] P. Sagaut, Large Eddy Simulation for Incompressible Flows, Springer, Berlin, 2001.
[42] U. Schumann, Subgrid scale model for finite difference simulation of turbulent flows in plane channels and annuli, J. Comput. Phys. 18 (1975) 376.
[43] J. Smagorinsky, General circulation experiments with the primitive equations: Part I. The basic experiment, Mon. Wea. Rev. 91 (1963) 99.
[44] P. Spalart, R. Moser, M. Rogers, Spectral methods for the Navier–Stokes equations with one infinite and two periodic directions, J. Comput. Phys. 96 (1991) 297.
[45] T. Wei, W.W. Willmarth, Reynolds-number effects on the structure of a turbulent channel flow, J. Fluid Mech. 204 (1989) 57.